

The energy cascade in grid-generated non-equilibrium decaying turbulence

P. C. Valente and J. C. Vassilicos

Citation: [Physics of Fluids \(1994-present\)](#) **27**, 045103 (2015); doi: 10.1063/1.4916628

View online: <http://dx.doi.org/10.1063/1.4916628>

View Table of Contents: <http://scitation.aip.org/content/aip/journal/pof2/27/4?ver=pdfcov>

Published by the [AIP Publishing](#)

Articles you may be interested in

[Relevance of turbulence behind the single square grid to turbulence generated by regular- and multiscale-grids](#)

Phys. Fluids **26**, 075105 (2014); 10.1063/1.4890746

[Experimental quantification of inverse energy cascade in deep rotating turbulence](#)

Phys. Fluids **25**, 085105 (2013); 10.1063/1.4817666

[Energy decay of rotating turbulence with confinement effects](#)

Phys. Fluids **18**, 065107 (2006); 10.1063/1.2212990

[Decaying grid-generated turbulence in a rotating tank](#)

Phys. Fluids **17**, 095105 (2005); 10.1063/1.2046710

[Inverse structure functions of temperature in grid-generated turbulence](#)

Phys. Fluids **16**, 2126 (2004); 10.1063/1.1710890

SHARE

your expertise in

simulation

TE11 cutoff frequency (fc): 4.888 Hz

Frequency: Hz

Wavelength (λ): m

Flare angle: °

Corrugation thickness: m


Corrugation length: m

Horn thickness: m

Horn length: m

Waveguide length: m

Matching corrugation length: m



WITH COMSOL APPS »

COMSOL

Input waveguide cross pol. ratio: 17.657 %

Output aperture cross pol. ratio: 3.025 %

☒ Target criterion: passed

The energy cascade in grid-generated non-equilibrium decaying turbulence

P. C. Valente^{1,2} and J. C. Vassilicos¹

¹*Department of Aeronautics, Imperial College London, London SW7 2AZ, United Kingdom*

²*LAETA/IDMEC, Instituto Superior Técnico, Universidade de Lisboa, 1049-001 Lisboa, Portugal*

(Received 9 October 2014; accepted 20 March 2015; published online 8 April 2015)

We investigate non-equilibrium turbulence where the non-dimensionalised dissipation coefficient C_ε scales as $C_\varepsilon \sim Re_M^m/Re_\ell^n$ with $m \approx 1 \approx n$ (Re_M and Re_ℓ are global/inlet and local Reynolds numbers, respectively) by measuring the downstream evolution of the scale-by-scale energy transfer, dissipation, advection, production, and transport in the lee of a square-mesh grid, and compare with a region where $C_\varepsilon \approx \text{constant}$. These are the main terms of the inhomogeneous, anisotropic version of the von Kármán-Howarth-Monin equation. It is shown in the grid-generated turbulence studied here that, even in the presence of non-negligible turbulence production and transport, production and transport are large-scale phenomena that do not contribute to the scale-by-scale balance for scales smaller than about a third of the integral-length scale, ℓ , and therefore do not affect the energy transfer to the small-scales. In both the non-equilibrium region where $C_\varepsilon \sim Re_M^m/Re_\ell^n$ and further downstream where $C_\varepsilon \approx \text{constant}$, the peak of the scale-by-scale energy transfer scales as $(\overline{u^2})^{3/2}/\ell$ ($\overline{u^2}$ is the variance of the longitudinal fluctuating velocity). In the non-equilibrium case, this scaling implies an imbalance between the energy transfer to the small scales and the dissipation. This imbalance is reflected on the small-scale advection which becomes larger in proportion to the maximum energy transfer as the turbulence decays whereas it stays proportionally constant in the further downstream region where $C_\varepsilon \approx \text{constant}$ even though Re_ℓ is lower. © 2015 AIP Publishing LLC. [<http://dx.doi.org/10.1063/1.4916628>]

I. INTRODUCTION

Recent work on fractal- and regular grid-generated decaying turbulence showed that there are two distinct turbulence decay regions demarcated by two different behaviours of the kinetic energy dissipation per unit volume, ε , at high Reynolds numbers.¹ A non-equilibrium region closer to the grid where $C_\varepsilon \equiv \varepsilon\ell/u'^3 \sim Re_M^m/Re_\ell^n$ (with $m \approx n \approx 1$ for the highest Reynolds number data), the local Reynolds number is high and the energy spectrum has a power law shape over a wide range of wavenumbers with exponent close to $-5/3$; and a region further downstream where the Reynolds number has dropped but $C_\varepsilon \sim \text{constant}$ (u' and ℓ are, respectively, the root-mean-square of the fluctuating velocity and an integral length-scale; $Re_\ell = u'\ell/\nu$ and $Re_M = U_\infty M/\nu$ with U_∞ being the inlet velocity, M an inlet mesh size, and ν the kinematic viscosity). This dichotomy of dissipation behaviours, and in particular the new non-equilibrium dissipation scalings, has been found with different measurement techniques and by different research groups²⁻⁷ (see review by Vassilicos¹) and recently on direct numerical simulations (DNSs) of homogeneous isotropic decaying turbulence.^{8,9}

In this paper, we attempt to flesh out the meaning and some of the properties of non-equilibrium turbulence and what distinguishes it from turbulence in the $C_\varepsilon \sim \text{constant}$ region. In particular, we want to investigate the connection between the non-equilibrium dissipation behaviour and the behaviour of the inertial energy cascade flux, Π ($C_\Pi \equiv \Pi\ell/u'^3$ in dimensionless terms). We do this on the basis of two-point two-component measurements which is the simplest configuration allowing the estimation of nearly all terms in the inhomogeneous and anisotropic form of the von Kármán-Howarth-Monin equation.¹⁰ These terms represent turbulent dissipation and scale-by-scale transport,

production, advection, energy transfer, and viscous diffusion. Such a detailed and systematic study of the scale by scale energy balance in grid-generated turbulence for either the non-equilibrium or the $C_\varepsilon \sim \text{constant}$ region was never reported in the literature. Furthermore, our data allow for the first time to assess the behaviour of Π in these complex flows which exhibit non-negligible departures from homogeneity and isotropy. Specially due to the latter, the usual isotropic surrogate for Π based on the longitudinal third-order structure functions is not satisfactory.¹¹

We chose to carry out this study in the lee of two regular grids, RG60 and RG115 (see Valente and Vassilicos¹²), for three reasons: (i) the new non-equilibrium dissipation law is most clearly defined in the lee of our regular grids; (ii) the far downstream $C_\varepsilon \sim \text{constant}$ law is accessible in our wind tunnels only with RG60; and (iii) the same test section region can be used to study non-equilibrium turbulence with RG115 and $C_\varepsilon \sim \text{constant}$ turbulence with RG60 (see Sec. III).

A. Balance between energy cascade and dissipation (Kolmogorov's 4/5th law)

In a seminal contribution, Kolmogorov¹³ arrived at an exact expression (i.e., without adjustable constants) relating the third-order structure function ($\overline{\delta u_\parallel^3}$) and the dissipation (ε) within the inertial-range. The starting point for the derivation is the von Kármán-Howarth equation,¹⁴ simplified using the framework put forward in his earlier work.¹⁵ The expression, $\overline{\delta u_\parallel^3} = -4/5 \varepsilon r$, is commonly known as Kolmogorov's 4/5th law due to the pre-factor appearing in the equation which follows from the hypothesis of local isotropy ($\overline{\delta u_\parallel(r)}$ is the component of the velocity difference parallel to the separation vector \mathbf{r} and $r = |\mathbf{r}|$). Note that one can relax the local isotropy constraint by averaging the third-order structure function over all solid angles and arrive to a more general "4/5th-type law."¹⁶ Since the third-order structure function is readily interpreted as a scale-by-scale (non-linear) energy flux, we refer to general "4/5th-type laws" as $\Pi - \varepsilon$ balance, where Π denotes the energy transfer in the inertial range ($\Pi = -5/4 d \overline{\delta u_\parallel^3}/dr$ in Kolmogorov's 4/5th-law). This balance and the related 4/5th-type laws represent the essence of the Richardson-Kolmogorov cascade.

Its importance can hardly be overstated since it serves as a basis of many theories and models of turbulence. This is readily identified whenever the dynamical role of the inertial range is characterised by a single scalar quantity, i.e., ε (including Kolmogorov's earlier work). Richardson's pair diffusion law and theories of acceleration-, pressure-, passive and active scalar-field characteristics in the inertial range¹⁷ are all examples of the implicit use of the dissipation as a measure of the instantaneous energy transfer across the inertial range and permitting a phenomenological theory to be constructed. Other related examples of the use of the $\Pi - \varepsilon$ balance, with some modifications, can be found in theories of polymer drag reduction¹⁸ and magnetohydrodynamics.¹⁹

For homogeneous stationary turbulence, the $\Pi - \varepsilon$ balance can be derived rigorously^{16,20} and has received substantial experimental and numerical support.²¹ However, the merit of Kolmogorov's work is the formulation of a theory for "the case of an arbitrary turbulent flow with sufficiently large Reynolds number"¹⁵ by introducing hypotheses of local homogeneity, local isotropy, and local stationarity. (Note that by local stationarity we are referring to Kolmogorov's idea that "within short time intervals [the small scale fluctuations] can naturally be regarded as being stationary, even when the flow as a whole is non-stationary"¹⁵—see also George²² for a critique of this concept.) So far, in the case of temporally or spatially evolving turbulent flows, the support of the $\Pi - \varepsilon$ balance is still meagre, arguably because the current laboratory and numerical experiments do not reach a sufficiently large Reynolds number for the onset of an inertial range.²¹ Still, in the above mentioned literature, there is a latent expectation that a $\Pi - \varepsilon$ balance will hold at extremely high Reynolds numbers, and the departures are broadly denoted as "finite Reynolds number" (FRN) effects.^{21,23–28}

In contrast with the above viewpoint, one can find literature (typically pertaining to turbulence modelling) questioning the validity of the instantaneous balance between energy transfer and dissipation in non-stationary and in spatially evolving flows^{29–32} and advocating the necessity to account for the transfer time of kinetic energy from large to small scales.^{29,30} In fact, there is neither local nor instantaneous balance between energy transfer and dissipation even in statistically stationary and homogeneous turbulence as pointed out by Kraichnan³³ and subsequently evidenced in direct numerical simulations by Borue and Orszag.³⁴ However, this balance does nevertheless hold on

average in statistically stationary and homogeneous turbulence if the Reynolds number is high enough but it does not in time-evolving (e.g., decaying) or spatially developing turbulence where the transfer time of kinetic energy from large to small scales, i.e., the time-lag, therefore becomes critically important in the description of the turbulence cascade.^{29–32,34–36}

We now proceed with the inhomogeneous and anisotropic form of the von Kármán-Howarth-Monin equation¹⁰ which forms the basis of the present study.

B. Scale-by-scale energy transfer budget equation

A scale-by-scale energy transfer budget similar to the von Kármán-Howarth-Monin equation (see Eq. 22.15 in Monin and Yaglom¹⁷), but extended to inhomogeneous turbulent flows, can be derived directly from the Navier-Stokes.^{10,37,38}

The starting point is the incompressible Navier-Stokes decomposed into mean and fluctuating components at two distinct locations, $\mathbf{x} \equiv \mathbf{X} + \mathbf{r}/2$ and $\mathbf{x}' \equiv \mathbf{X} - \mathbf{r}/2$ (\mathbf{X} is the centroid of the two points and $r = |\mathbf{r}|$ their distance),

$$\left\{ \begin{aligned} & \frac{\partial U_i + u_i}{\partial t} + U_k \frac{\partial u_i}{\partial x_k} + u_k \frac{\partial U_i}{\partial x_k} + U_k \frac{\partial U_i}{\partial x_k} + u_k \frac{\partial u_i}{\partial x_k} = \\ & \quad - \frac{1}{\rho} \frac{\partial P + p}{\partial x_i} + \nu \frac{\partial^2 U_i + u_i}{\partial x_k^2} \\ & \frac{\partial U'_i + u'_i}{\partial t} + U'_k \frac{\partial u'_i}{\partial x'_k} + u'_k \frac{\partial U'_i}{\partial x'_k} + U'_k \frac{\partial U'_i}{\partial x'_k} + u'_k \frac{\partial u'_i}{\partial x'_k} = \\ & \quad - \frac{1}{\rho} \frac{\partial P' + p'}{\partial x'_i} + \nu \frac{\partial^2 U'_i + u'_i}{\partial x'^2_k}, \end{aligned} \right. \quad (1)$$

together with the continuity equations ($\partial U_k / \partial x_k = \partial U'_k / \partial x'_k = \partial u_k / \partial x_k = \partial u'_k / \partial x'_k = 0$). In the present notation, $U_i \equiv U_i(\mathbf{x})$, $u_i \equiv u_i(\mathbf{x})$, $P \equiv P(\mathbf{x})$, $U'_i \equiv U'_i(\mathbf{x}')$, $u'_i \equiv u'_i(\mathbf{x}')$, and $P' \equiv P(\mathbf{x}')$.

The main steps in the derivation are to (i) subtract the two equations above and denote the velocity differences as $\delta u_i \equiv u_i - u'_i$, $\delta p \equiv p - p'$, and $\delta U_i \equiv U_i - U'_i$, (ii) multiply the resulting expression by $2\delta u_i$, (iii) ensemble average over an infinite number of realisations (denoted by overbars; in practice, ergodicity is used on the basis of the time stationarity at a given point in our spatially evolving flows and time averages are performed), and (iv) change the coordinate system from $(\mathbf{x}, \mathbf{x}')$ to (\mathbf{X}, \mathbf{r}) . The resulting equation reads

$$\begin{aligned} & \frac{\partial \overline{\delta q^2}}{\partial t} + \left(\frac{U_k + U'_k}{2} \right) \frac{\partial \overline{\delta q^2}}{\partial X_k} + \frac{\partial \overline{\delta u_k \delta q^2}}{\partial r_k} + \frac{\partial \overline{\delta U_k \delta q^2}}{\partial r_k} = \\ & \quad - 2 \overline{\delta u_i \delta u_k} \frac{\partial \delta U_i}{\partial r_k} - \overline{(u_k + u'_k) \delta u_i} \frac{\partial \delta U_i}{\partial X_k} - \\ & \quad \frac{\partial}{\partial X_k} \left(\frac{(u_k + u'_k) \delta q^2}{2} \right) - \frac{2}{\rho} \frac{\partial \overline{\delta u_k \delta p}}{\partial X_k} + \\ & \quad \nu \left[2 \frac{\partial^2}{\partial r_k^2} + \frac{1}{2} \frac{\partial^2}{\partial X_k^2} \right] \overline{\delta q^2} - 2\nu \left[\overline{\left(\frac{\partial u_i}{\partial x_k} \right)^2} + \overline{\left(\frac{\partial u'_i}{\partial x'_k} \right)^2} \right], \end{aligned} \quad (2)$$

where $\overline{\delta q^2} \equiv \overline{(\delta u_i)^2}$ (with summation over the index $i = 1, 2, 3$). Equation (2) is essentially an inhomogeneous von Kármán-Howarth-Monin equation with additional terms to account for the inhomogeneity of the turbulent flow field. Each of the terms can be interpreted as follows.

1. $4\mathcal{A}_t^*(\mathbf{X}, \mathbf{r}) \equiv \partial \overline{\delta q^2} / \partial t$ results from the time dependence that $\overline{\delta q^2}(\mathbf{X}, \mathbf{r})$ can have in certain unsteady flows.
2. $4\mathcal{A}^*(\mathbf{X}, \mathbf{r}) \equiv (U_k + U'_k) / 2 \partial \overline{\delta q^2} / \partial X_k$ represents an advection contribution to the change of $\overline{\delta q^2}(\mathbf{X}, \mathbf{r})$.

3. $4\Pi^*(\mathbf{X}, \mathbf{r}) \equiv \partial \overline{\delta u_k \delta q^2} / \partial r_k$ represents a contribution which relates to nonlinear transfer of energy from the orientation point \mathbf{r}/r on a spherical shell of radius r centred at \mathbf{X} to (a) concentric shells of larger radii (effectively to smaller radii since this term is typically negative) and (b) to other orientations within the same spherical shell. Notice that Π^* is the divergence with respect to \mathbf{r} of the flux $\overline{\delta u_k \delta q^2}$ and that owing to Gauss's theorem, if the turbulence is homogeneous, the radial flux is zero in the limit $r \rightarrow \infty$ and $4\Pi^*$ is indeed, unequivocally, a transfer term. Also note that (using a spherical coordinate system (r, θ, ϕ) for \mathbf{r}) the integrals of the polar, Π_θ^* , and azimuthal, Π_ϕ^* , contributions to the divergence Π^* over the solid angle \mathbf{r}/r are identically zero.
4. $4\Pi_U^*(\mathbf{X}, \mathbf{r}) \equiv \partial \delta U_k \overline{\delta q^2} / \partial r_k$ represents a contribution which relates to linear transfer of energy by mean velocity gradients from the orientation point \mathbf{r}/r on a spherical shell of radius r centred at \mathbf{X} to concentric shells of larger radii. The motivation for this interpretation is analogous to that given for Π^* , where the turbulent flux is now $\delta U_k \overline{\delta q^2}$ (see also Deissler^{37,39} where the physical interpretation of this term is given in wavenumber space).
5. $4\mathcal{P}^*(\mathbf{X}, \mathbf{r}) \equiv -2\overline{\delta u_i \delta u_k} \partial \delta U_i / \partial r_k - (\overline{u_k + u'_k}) \delta u_i \partial \delta U_i / \partial X_k$ represents a contribution which relates to turbulent production. It is easiest to identify \mathcal{P}^* as a production term by writing it in $(\mathbf{x}, \mathbf{x}')$ coordinates, i.e., $2\mathcal{P}^* = -\overline{u_i u_k} \partial U_i / \partial x_k - \overline{u'_i u'_k} \partial U'_i / \partial x'_k + \overline{u_i u'_k} \partial U_i / \partial x_k + \overline{u'_i u_k} \partial U'_i / \partial x'_k$, and recognising that the first two terms on the right-hand side are the usual production terms of the single-point turbulent kinetic energy transport equation evaluated at \mathbf{x} and \mathbf{x}' , respectively.
6. $4\mathcal{T}^*(\mathbf{X}, \mathbf{r}) \equiv -\partial / \partial X_k \left(\overline{(u_k + u'_k) \delta q^2} / 2 + 2/\rho \overline{\delta u_k \delta p} \right)$ represents scale-by-scale turbulent transport from the orientation point \mathbf{r}/r on a spherical shell of radius r centred at \mathbf{X} to an adjacent shell (centred at $\mathbf{X} + \delta \mathbf{X}$) with the same radius and at the same orientation. Notice that \mathcal{T}^* is the divergence with respect to \mathbf{X} of the flux $-\overline{(u_k + u'_k) \delta q^2} / 2 - 2/\rho \overline{\delta u_k \delta p}$ and thus, making use of Gauss's theorem, it follows that the net contribution of \mathcal{T}^* integrated (with respect to \mathbf{X} for each \mathbf{r}) over a volume V is equal to the total flux over the bounding surface of V . This motivates the physical interpretation of this term as a scale-by-scale turbulent transport.
7. $4\mathcal{D}_v^*(\mathbf{X}, \mathbf{r}) \equiv 2\nu \partial^2 \overline{\delta q^2} / \partial r_k^2$ represents viscous diffusion around the orientation point \mathbf{r}/r on a spherical shell of radius r centred at \mathbf{X} (note that $\lim_{r \rightarrow 0} \mathcal{D}_v^*(\mathbf{X}, \mathbf{r}) = \varepsilon(\mathbf{X})$).
8. $4\mathcal{D}_{X,v}^*(\mathbf{X}, \mathbf{r}) \equiv \nu/2 \partial^2 \overline{\delta q^2} / \partial X_k^2$ represents scale-by-scale transport via viscous diffusion around the orientation point \mathbf{r}/r on a spherical shell of radius r centred at \mathbf{X} . This can be seen as a transport term following the same reasoning as that made for \mathcal{T}^* by noticing that $4\mathcal{D}_{X,v}^*$ can be written as a divergence of the viscous flux $\nu/2 \partial \overline{\delta q^2} / \partial X_k$.
9. $4\varepsilon^*(\mathbf{X}, \mathbf{r}) \equiv 2\nu (\partial u_i / \partial x_k)^2 + 2\nu (\partial u'_i / \partial x'_k)^2$ represents the sum of twice the turbulent kinetic energy dissipation at the two locations, i.e., $2\varepsilon + 2\varepsilon' = 4\varepsilon^*$ with $\varepsilon^* \equiv (\varepsilon + \varepsilon')/2$, where $\varepsilon = \overline{(\partial u_i / \partial x_k)^2}$ and $\varepsilon' = \overline{(\partial u'_i / \partial x'_k)^2}$.

For large enough r , Eq. (2) reduces to four times the average of two single-point turbulent kinetic energy transport equations, one evaluated at \mathbf{x} and the other at \mathbf{x}' .³⁸ Recall that the dependence on the orientation \mathbf{r}/r can be removed by averaging the terms over spherical shells of radius r , in the spirit of Nie and Tanveer.¹⁶ The spherical shell averaged terms are denoted by removing the superscript asterisk.

C. Outline

This paper is organised as follows. In Sec. II, the details of the experimental apparatus are presented together with all the necessary *a priori* checks to ensure the quality of the collected data. In Sec. III, we specify how each of the terms in (2) is estimated from the data and discuss the downstream variation in the anisotropy of the two-point second- and third-order structure functions. In Sec. IV, we discuss the role of turbulence production and transport on the other terms in (2). In Sec. V we discuss the scaling of the scale-by-scale energy transfer, advection, and viscous diffusion as the flow decays for both the non-equilibrium and the $C_\varepsilon \sim \text{constant}$ regions and summarize the main findings in Sec. VI.

II. EXPERIMENTAL SETUP

A. Measurement apparatus

The experiments are performed in a $0.46\text{ m} \times 0.46\text{ m} \times 3.5\text{ m}$ blow-down wind tunnel at the Department of Aeronautics in Imperial College London^{12,40} (see Fig. 1(a)).

The measurement apparatus to compute estimates of the terms in Eq. (2) (except the pressure transport term) consists of two X-probes (aligned with the xy plane to measure the longitudinal and vertical velocity components, U and V for the mean, and u , v for the fluctuating components) mounted on a traverse mechanism controlling the vertical distance between the probes and their individual pitch angle for *in-situ* calibration (see Figs. 1(b) and 1(c)). (Note that, in the orthonormal coordinate system used, x is aligned with the mean flow, and y and z are perpendicular and parallel

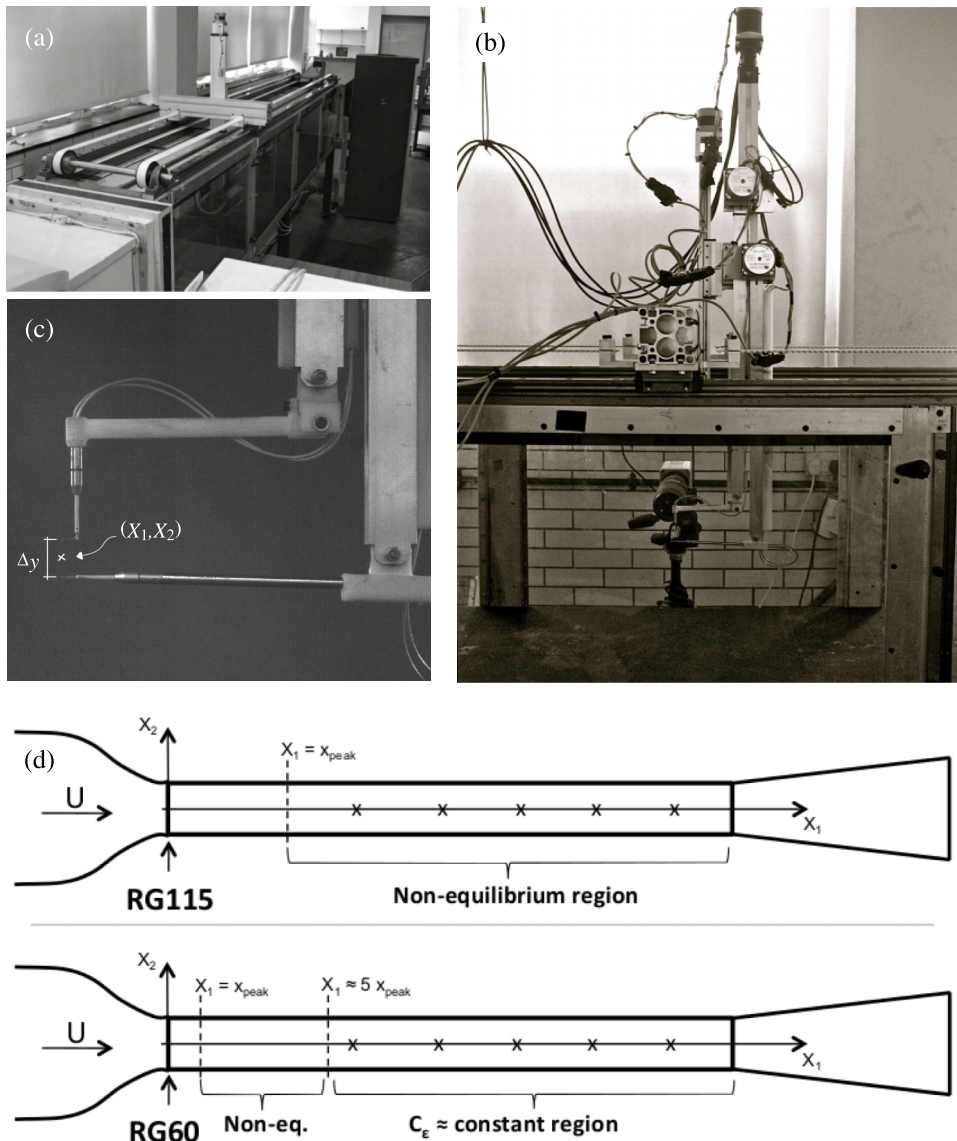


FIG. 1. Measurement apparatus. (a) Photo of $18'' \times 18''$ wind tunnel, (b) traverse mechanisms for the two-component/two-point measurements, (c) close-up on the probe holders, and (d) sketch of the wind tunnel with the approximate extent of the non-equilibrium and $C_\epsilon \sim \text{constant}$ regions for the turbulence generated by two grids used, RG60 and RG115. The centroids of the five measurement locations are represented in (d) where it can be seen that they correspond to a non-equilibrium region at the lee of RG115 and to a $C_\epsilon \sim \text{constant}$ region at the lee of RG60.

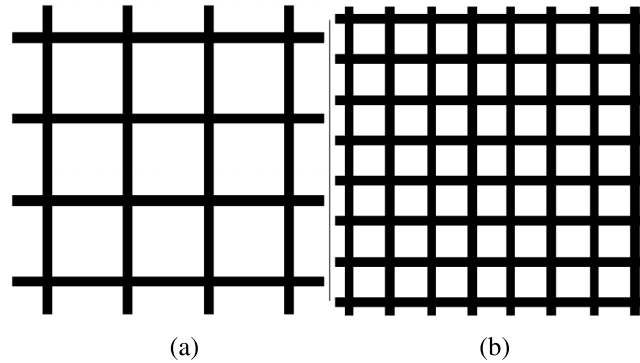


FIG. 2. Sketch of the turbulence generating grids, (a) RG115 and (b) RG60. The RG115 is a mono-planar regular grid with a distance between parallel bars of $M = 115$ mm, lateral and longitudinal bar thicknesses of $t_0 = 10$ mm and $d = 3.2$ mm, respectively, and a blockage ratio of $\sigma = 17\%$. The RG60 is a bi-planar regular grid with $M = 60$ mm, $t_0 = d = 10$ mm, and $\sigma = 32\%$. Owing to the geometrical differences between the RG115 and RG60, the location of the turbulent kinetic energy peak along the centreline ($y = z = 0$) is considerably different: $x_{\text{peak}} \approx 0.83$ m and $x_{\text{peak}} \approx 0.14$ m, respectively.

to the floor, respectively, see Fig. 1(d).) Data are acquired in the lee of two regular grids, RG115 and RG60, sketched in Fig. 2 and described in the caption of the figure.

This apparatus was previously used to measure two transverse velocity correlation functions⁴¹ where a detailed description of the traverse and measurement systems can be found together with an assessment of the measurement resolution and mutual interference between the two X-probes. For convenience, we recall that one of the vertical traverse systems displaces the two probes symmetrically about their centroid (defined as the geometrical midpoint between the X-probes' centres) whereas the second vertical traverse system displaces the centroid keeping the separation between the probes fixed (see Fig. 1(c)). For short probe separations, the distance between the X-probes is optically measured with an external camera which is used to set the reference separation as well as to ensure high position accuracy (see Fig. 1(b)). The minimum vertical separation between the probes is $\Delta y = 1.2$ mm (probe resolution $\sim 4\eta - 8\eta$), whereas the maximum separation in the measurements is 70 mm ($\sim 2L$). In total, 23 separations are measured ($\Delta y = 1.2, 1.6, 2.0, 2.5, 3.0, 3.5, 4.5, 6, 8, 10, 12, 14, 16, 20, 24, 28, 32, 36, 44, 52, 60, 70$ mm). It was found that the overall precision of the prescribed vertical separation between the X-probes was typically ± 50 μm (i.e., over the three degrees of freedom: vertical symmetric displacement and pitching of the two individual probes used for calibration).

B. Data acquisition and statistical convergence

The in-built signal conditioners of the anemometer are set to analogically filter at 30 kHz and to offset and amplify the signal -1 V and $2\times$, respectively. The four analogue anemometer signals are sampled at 62.5 kHz with a National Instruments NI-6229 (USB) with a resolution of 16-bit over a range of $[-1, 1]$ V. The turbulent velocity signals are acquired for 9 min corresponding to 150 000 – 200 000 integral-time scales. The data acquisition, wind tunnel speed, and traverse motors control are performed with MATLABTM.

Perhaps the most demanding statistic of interest here, in terms of statistical convergence, is the triple structure function $\overline{\delta u_i \delta q^2}$. To quantify its statistical uncertainty, we assign 95% confidence intervals to the measurements.⁴² The sampling variance ($\text{var}(\delta u_i \delta q^2)$) is estimated as

$$\text{var}(\delta u_i \delta q^2) = \frac{1}{N} \left(\overline{(\delta u_i \delta q^2)^2} - \overline{\delta u_i \delta q^2}^2 \right), \quad (3)$$

where N is the number of independent samples. (Note that $\overline{\delta u_i \delta q^2}$ is non-central statistical moment, hence Eq. (4) of Benedict and Gould,⁴² which is derived for central moments, has additional uncertainty terms which are not applicable, see Ref. 43 for further details.)

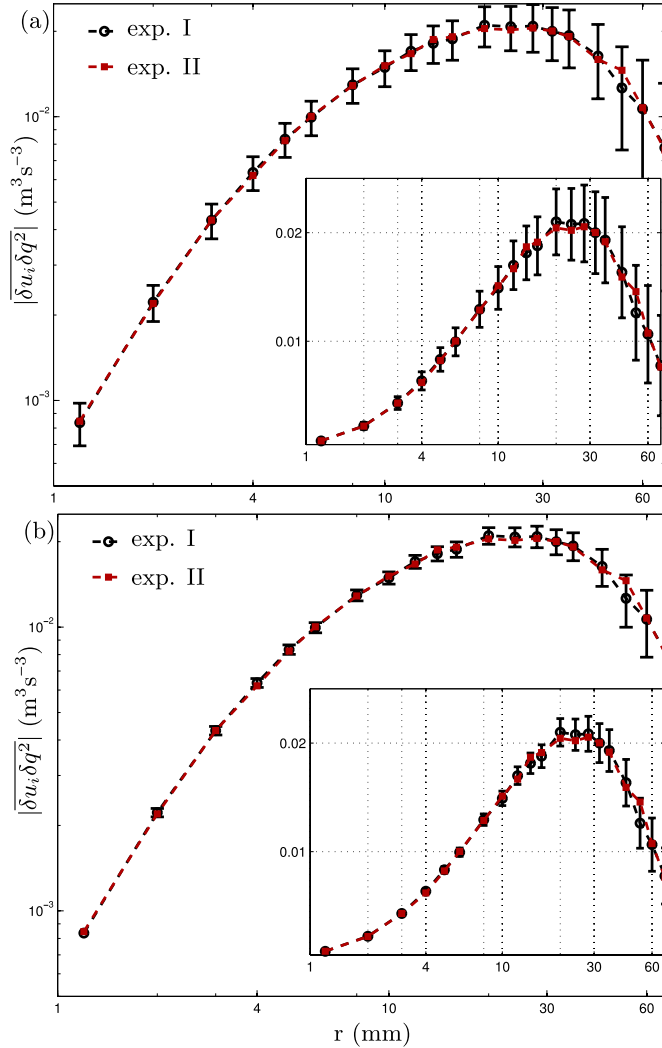


FIG. 3. Third order structure function $|\overline{\delta u_i \delta q^2}|$ versus the transverse separations $(r_x, r_y) = (0, r)$ with 95% confidence intervals estimated with (a) the global integral time-scale and (b) a tailored integral time-scale characteristic of $\overline{\delta u_i \delta q^2}(r_x, r_y)$ (data acquired at the lee of RG60 for the centroid at $(x, y, z) = (1250, 0, 0)$ mm in a precursory experiment). The same experiment is repeated twice to show the repeatability of the results and to support the fact that 95% confidence intervals estimated with a tailored integral time-scale are a better estimate for the statistical uncertainty. The data are shown in logarithmically spaced abscissae and ordinates. In the insets, the same data are shown using linear ordinates.

The repeatability of the measurement of $\overline{\delta u_i \delta q^2}$ was also assessed in a precursory experiment by repeating the same measurement twice (data acquired at the lee of RG60 for the centroid at $(x, y, z) = (1250, 0, 0)$ mm). Comparing the repeatability (a somewhat more stringent test) with the estimated uncertainty (Fig. 3(a)), we notice that the confidence intervals are excessively large. This could indicate that the number of independent samples, N , based on the integral-time scale, is underestimated. Indeed, splitting the data into integral-time scale sized blocks and extracting a single sample of $\delta u_i \delta q^2(r_x, r_y)$ leads to estimates of $\delta u_i \delta q^2(r_x, r_y)$ with significantly more scatter, indicating that uncorrelated samples were lost. Instead of using the standard integral time-scale, we can define alternative de-correlation time-scales by taking the autocorrelation of $\delta u_i \delta q^2(r_x, r_y)$ at two times with varying lags and then integrating the resulting correlation functions. This methodology provides a tailored integral time-scale representative of the de-correlation length associated with $\delta u_i \delta q^2$ at each (r_x, r_y) . Assuming that twice this tailored integral time-scale is the characteristic lag between independent samples of $\delta u_i \delta q^2(r_x, r_y)$, we get new estimates of $N(r_x, r_y)$ and

consequently new confidence intervals, which are shown in Fig. 3(b). Note that, experiments performed with particle imaging velocimetry (PIV)^{10,44} obtain reasonable estimates of $\overline{\delta u_i \delta q^2}$ even though the number of independent samples is $\mathcal{O}(10^3)$.

The error bars of the spherically averaged divergence of $\overline{\delta u_i \delta q^2}$ (Figs. 8-13) include the 95% confidence intervals plus the error due to the uncertainty of the vertical separation between the X-probe $\approx \pm 50 \mu\text{m}$ (see Sec. II A). The two uncertainties are stacked with a standard propagation of error formula applied to the central differences scheme. When this quantity is normalised by ε (Figs. 9-11), the uncertainty of the dissipation estimate is also stacked to the error bars with a standard propagation of error formula.

III. DESCRIPTION OF THE EXPERIMENTAL RESULTS

The data are acquired with **X**, the midpoint between the two X-probes, along the centreline ($y = z = 0$) at five downstream locations between $x = 1250 \text{ mm}$ and $x = 3050 \text{ mm}$ ($X_1 = 1250, 1700, 2150, 2600, 3050 \text{ mm}$ and $X_2 = X_3 = 0$). For two downstream locations of the centroid, $X_1 = 1250 \text{ mm}$ and $X_1 = 2150 \text{ mm}$, additional datasets off-centreline at $X_2 = -6 \text{ mm}$ and $X_3 = 0$ are acquired so that derivatives of the statistics with respect to X_2 can be computed, particularly those needed to estimate $\partial/\partial X_2 (\overline{v + v'}) \delta q^2$, see Eq. (2). The choice of 6 mm as the distance to evaluate the X_2 -derivative is based on the single-point data in the lee of RG115-turbulence used in Valente and Vassilicos⁴¹ to estimate the lateral triple-correlation transport (i.e., $\partial/\partial y \overline{v q^2}$). Based on those data, it is found that the spanwise derivative $\partial/\partial y \overline{v q^2}$ is well approximated by $(\overline{v q^2}(h_y) - \overline{v q^2}(0))/h_y$ up to spacings of $h_y \approx 8 \text{ mm}$. Too small h_y introduce unnecessary uncertainty to the estimates.

Recall that the X-probes are symmetrically traversed in the y-direction with respect to a fixed **X**, thus enabling the measurement of the statistical correlations as a function of r_2 , and that the dependence on r_1 is recovered using Taylor's hypothesis. On the other hand, the traverse mechanism does not allow displacements in the z-direction, and the measurements are restricted to the vertical xy-plane at $z = 0$ and thus $X_3 = 0$ and $r_3 = 0$.

The downstream range of the measurements corresponds to $8 - 21x_{\text{peak}}$ for RG60 and $1.5 - 3.7x_{\text{peak}}$ for RG115, a stark difference in the streamwise range relative to x_{peak} owing to the geometrical differences between the grids (see Fig. 2). From previous experiments with these grids,^{12,41} we know that the non-equilibrium region at the lee of RG115 extends at least up to $3.8x_{\text{peak}}$ and the $C_\varepsilon \sim \text{constant}$ region at the lee of RG60 starts at $5x_{\text{peak}}$. Therefore, the measurement range for the RG115 corresponds to a nonclassical energy dissipation region whereas for the RG60 it corresponds to a $C_\varepsilon \sim \text{constant}$ one, thus allowing their direct comparison. Recall that the Re_λ ranges, as well as the straddled Kolmogorov microscales η , are comparable for both grids at the chosen measurement locations. Hence, the same setup can be used in both experiments without penalising resolution ($84 \leq Re_\lambda \leq 100$ versus $105 \leq Re_\lambda \leq 140$ and $0.19 \text{ mm} \leq \eta \leq 0.32 \text{ mm}$ versus $0.16 \text{ mm} \leq \eta \leq 0.28 \text{ mm}$ for RG60- and RG115-generated turbulence, respectively).

Note that the Taylor microscale is calculated as $\lambda = (15\nu \overline{u^2}/\varepsilon)^{1/2}$ and the Kolmogorov microscale as $\eta = (\nu^3/\varepsilon)^{1/4}$. The longitudinal integral length-scale is calculated as $L_{11}^{(1)} = 1/\overline{u^2} \int_0^\infty \overline{u(X_1 - r_1/2)u(X_1 + r_1/2)} dr_1$ (see Ref. 41 for further details). The dissipation rate is estimated as $\varepsilon = \varepsilon^{\text{iso},3} \equiv \nu((\partial u/\partial x)^2 + 2(\partial v/\partial x)^2 + 4(\partial u/\partial y)^2 + 2(\partial v/\partial y)^2)$ and compensated for the bias induced by the finite spacing between the adjacent probes used to measure $\partial u/\partial y$ and $\partial v/\partial y$. Since our datasets contain data with different (small) spacings between the probes, we obtained several compensated estimates for ε , and their variability is presented in the numerical values of ε in Tables I and II (see Sec. 5 of Ref. 41 for further details).

A. Estimation of the terms in the inhomogeneous Kármán-Howarth-Monin equation

We now describe how the terms appearing in inhomogeneous Kármán-Howarth-Monin equation (2) are estimated from the present two-component, two-dimensional data using the statistical characteristics of the flow and some additional assumptions.

TABLE I. Single point turbulence statistics for the RG60 along the centreline (see main text for the methodology used to estimate the quantities).

Location	1250	1700	2150	2600	3050
x/x_{peak}	8.5	11.5	15.6	17.6	20.7
Re_λ	100	94	89	87	84
$\overline{u^2}$ (m ² s ⁻²)	0.15	0.10	0.07	0.06	0.05
$L_{11}^{(1)}$ (mm)	29.3	32.5	35.0	36.6	39.4
λ (mm)	3.8	4.4	5.0	5.5	5.8
η (mm)	0.19	0.23	0.27	0.30	0.32
ε (m ² s ⁻³)	2.51 ± 0.07	1.18 ± 0.02	0.66 ± 0.02	0.42 ± 0.01	0.30 ± 0.01

From the spatially varying two-component turbulent signals, acquired simultaneously at the 23 transverse separations, the second- and third-order structure functions $\overline{(\delta u)^2}$, $\overline{(\delta v)^2}$, $\overline{(\delta u)^3}$, $\overline{(\delta v)^3}$, $\overline{\delta u(\delta v)^2}$, $\overline{\delta v(\delta u)^2}$ and the mixed structure functions $\overline{(v+v')\delta u}$, $\overline{(u+u')(\delta u)^2}$, $\overline{(v+v')(\delta u)^2}$, $\overline{(u+u')(\delta v)^2}$, $\overline{(v+v')(\delta v)^2}$ are computed for all (r_1, r_2) . (Note that r_2 are just the 23 transverse separations ($1.2 \text{ mm} \leq \Delta y \leq 70 \text{ mm}$) and $r_1 = n_i f_s/U_\infty$ where f_s/U_∞ is the spatial sampling frequency by virtue of Taylor's hypothesis, and n_i are 23 integers chosen to yield approximately the same separation magnitudes as those in the transverse direction.)

The structure functions are then bi-linearly interpolated onto a spherical coordinate system $(r, \theta, \phi = 0)$ such that $(r, 0, 0)$ is aligned with r_1 and $(r, \pi/2, 0)$ with r_2 (see Fig. 4). The grid points in the new coordinate system are located at the interceptions between the 23 circumferences of radius r and 19 equally spaced radial lines between the polar angles, $\theta = [0 \ \pi/2]$. After the interpolation, the data are smoothed with a weighted average between each data point at (r, θ) and its neighbours $(r \pm \Delta r, \theta \pm \Delta \theta)$ (the total weight of the neighbouring points amounts to 37.5%).

The greatest limitation of the present measurements is lacking the data for the third velocity component, w . Lamriben, Cortet, and Moisy⁴⁴ faced the same limitation in their PIV data which they negotiated by considering the two-component surrogates of the structure functions, which may be sufficient to make qualitative inferences. However, the aim here is to obtain quantitative estimates of the terms in Eq. (2). This is achieved by assuming inter-component axisymmetry of the velocity-difference statistics relative to the \mathbf{r} -axis. In other words, it is assumed that the statistics of the two velocity-difference components perpendicular to $\mathbf{r} = (r_1, r_2, 0)$ (δu_\perp and δu_+ , see Fig. 4) are approximately equal. For the second-order structure function, this assumption leads to $\overline{(\delta q)^2}(\mathbf{r}) = \overline{(\delta u_\parallel)^2} + 2\overline{(\delta u_\perp)^2}$. Similarly, for the third-order structure functions, $\overline{\delta u_i(\delta q)^2}(\mathbf{r}) = \overline{\delta u_i(\delta u_\parallel)^2} + 2\overline{\delta u_i(\delta u_\perp)^2}$ and $\overline{(u_i + u'_i)(\delta q)^2}(\mathbf{r}) = \overline{(u_i + u'_i)(\delta u_\parallel)^2} + 2\overline{(u_i + u'_i)(\delta u_\perp)^2}$. Note that this assumption is weaker than complete isotropy as it allows for dependence on the orientation \mathbf{r}/r . Nevertheless, there are no presently available data to substantiate this assumption and therefore their validity requires further investigation. Even so, it has been verified against all the present data that the added component (i.e., the factor of 2 in the equalities two sentences above) does not change the qualitative behaviour of the structure functions, only their magnitude.

TABLE II. Single point turbulence statistics for the RG115 along the centreline (see main text for the methodology used to estimate the quantities).

Location	1250	1700	2150	2600	3050
x/x_{peak}	1.5	2.0	2.6	3.1	3.7
Re_λ	140	126	118	110	105
$\overline{u^2}$ (m ² s ⁻²)	0.32	0.20	0.14	0.10	0.08
$L_{11}^{(1)}$ (mm)	28.6	30.7	34.5	37.8	40.9
λ (mm)	3.7	4.2	4.7	5.1	5.6
η (mm)	0.16	0.19	0.22	0.25	0.28
ε (m ² s ⁻³)	5.21 ± 0.24	2.59 ± 0.12	1.48 ± 0.02	0.89 ± 0.02	0.55 ± 0.04

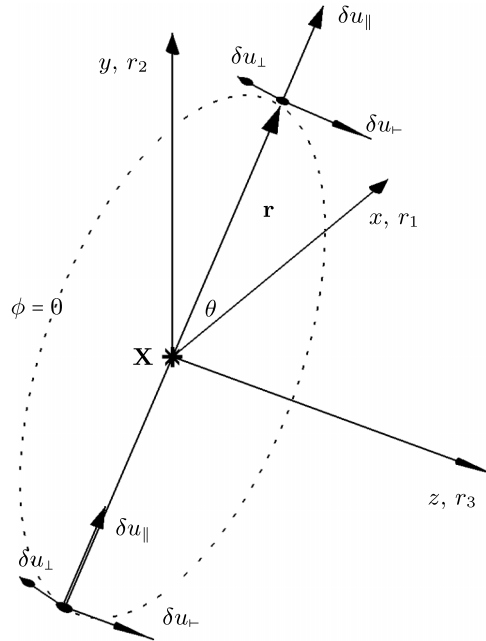


FIG. 4. Sketch of the three velocity-difference components (δu_{\parallel} , δu_{\perp} , δu_r). δu_{\parallel} and δu_{\perp} are the velocity-difference components lying in the measurement plane ($r_3 = 0$) which are, respectively, parallel and perpendicular to the separation vector \mathbf{r} . δu_r is the velocity-difference component orthogonal to the other two (δu_r). In the spherical coordinate system used here, θ is the angle between \mathbf{r} and the r_1 -axis, and $\phi = 0$ corresponds to the r_1 - r_2 plane.

Using the processed data, each of the terms in Eq. (2), except the pressure transport, is estimated at the measurement plane as follows. Note that the numerical derivatives, both first and second orders, are computed using a three-point, non-equally spaced central differences scheme.⁴⁵ For equally spaced derivatives, this algorithm returns the usual standard central differences scheme.

- $\mathcal{A}_t^* = 0$ since grid-generated turbulence is stationary in the Eulerian frame.
- $4\mathcal{A}^* \approx (U + U')/2 \partial/\partial X_1 \overline{\delta q^2}$ since the mean flow is approximately parallel, $V \approx W \approx 0$, and consequently, the advection in the y- and z-directions is negligible. The streamwise derivatives $\partial/\partial X_1 \overline{\delta q^2}$ are actually computed as $\overline{\delta q^2}/X_1 \partial/\partial \log X_1 (\log \overline{\delta q^2})$ using the three-point central differences' scheme referenced above. Consequently, we use three datasets at different X_1 to compute the advection at each X_1 for all r (recall that there are a total of five datasets with $X_1 = 1250, 1700, 2150, 2600$, and 3050 mm, respectively). Even though the various X_1 are coarsely spaced, it has been verified against the present data that the decay of $\overline{\delta q^2}$ for every r can be reasonably approximated with a power-law whose virtual origin coincides with the location of the grid (just as a check of the formula used to compute streamwise derivatives). Also, the longitudinal gradients of the mean velocity are small and therefore, we make use of $(U + U')/2 \approx (U(X_1, X_2 + r_2/2, 0) + U(X_1, X_2 - r_2/2, 0))/2$ to calculate $(U + U')/2 = (U(X_1 + r_1/2, X_2 + r_2/2, 0) + U(X_1 - r_1/2, X_2 - r_2/2, 0))/2$.
- $4\Pi^* \approx 1/r^2 \partial/\partial r (r^2 \overline{\delta u_{\parallel} \delta q^2}) + 1/(r \sin \theta) \times \partial/\partial \theta (\overline{\delta u_{\perp} \delta q^2})$, i.e., the divergence is computed in the spherical coordinate system, and the azimuthal component is assumed to be negligible owing to the axisymmetry of the turbulence statistics with respect to the centreline (see discussion at the end of this subsection). Future work will be required to assess this assumption.
- $\Pi_U^* \approx r_1 \partial U/\partial x \partial/\partial r_1 (\overline{\delta q^2}) \approx 0$ see Appendix A.
- $4\mathcal{P}^* \approx 2(\overline{\delta u})^2 \partial U/\partial x + 4(\overline{v + v'}) \overline{\delta u} \partial U/\partial y$ since $V \approx W \approx 0$ and $\partial U/\partial z = \partial U'/\partial z' \approx 0$ due to the expected symmetry of the mean flow relative to the plane $z = 0$ which is parallel to the tunnel's vertical walls, includes the centreline, and cuts the tunnel longitudinally in half. Also note that the symmetry of the mean flow relative to the centreline (leading to $\partial U/\partial x \approx \partial U'/\partial x'$,

$\partial U/\partial y \approx -\partial U'/\partial y')$ has been used to simplify $\partial \delta U/\partial r_k = 1/2(\partial U/\partial x_k + \partial U'/\partial x'_k)$ as $\partial U/\partial x$ and $\partial \delta U/\partial X_k = \partial U/\partial x_k - \partial U'/\partial x'_k$ as $2\partial U/\partial y$. The transverse gradient $\partial U/\partial y$ is taken from a 12th-order polynomial fit to the mean velocity data at each X_1 , and the longitudinal gradient $\partial U/\partial x$ is computed as described in the previous item.

- $4\mathcal{T}^* \approx -\partial/\partial X_1 \left(\overline{(u+u')\delta q^2/2} \right) - \partial/\partial X_2 \left(\overline{(v+v')\delta q^2} \right) - 4\mathcal{T}_p^*$. The transverse derivative $\partial/\partial X_2 \left(\overline{(v+v')\delta q^2/2} \right) (\approx \partial/\partial X_3 \left(\overline{(w+w')\delta q^2/2} \right))$ owing to the symmetry of the turbulence statistics to 90° rotations because of the grid's geometry) is only computed where the additional off-centreline measurements are acquired. The transverse derivative is simply taken as the difference between centreline and off-centreline data divided by their distance. The derivative with respect to X_1 is computed using the various datasets with different X_1 . However, this can only be considered as a rough approximation since the various X_1 are coarsely spaced. Nevertheless, the longitudinal turbulent transport is typically a small fraction of the lateral transport as was checked against the present two-point data as well as against the single-point transport data presented in Sec. 3 of Ref. 41. The pressure transport, \mathcal{T}_p^* , data cannot be directly estimated with the present apparatus. However, there is no *a priori* reason to consider it negligible and therefore it is retained in Eq. (2) as an unknown. Nevertheless, the contribution from \mathcal{T}_p^* can be inferred indirectly from the deviations of the measured terms' balance via Eq. (2).
- $4\mathcal{D}_v^* \approx 2\nu/r^2 \partial/\partial r \left(r^2 \partial/\partial r \left(\overline{\delta q^2} \right) \right)$, i.e., only the radial component of the Laplacian is computed. Note that the integrals of the polar, $\mathcal{D}_{v,\theta}^*$, and azimuthal, $\mathcal{D}_{v,\phi}^*$, components of the Laplacian over a spherical shell are identically zero. Only spherical shell averages (effectively circumferential averages) are discussed below and therefore the polar and azimuthal components are not computed.
- $4\mathcal{D}_{X,v}^* \approx \nu/2 \partial^2/\partial X_1^2 \left(\overline{\delta q^2} \right) + \nu/2 \partial^2/\partial X_2^2 \left(\overline{\delta q^2} \right) \approx 0$, see Appendix A.
- $4\varepsilon^* \approx 4\varepsilon^{\text{iso},3}$, i.e., the centreline energy dissipation estimate $\varepsilon^{\text{iso},3}$ is used as a surrogate for the average of the actual dissipation at \mathbf{x} and \mathbf{x}' (see Sec. 5 in Ref. 41 where the different dissipation estimates are discussed). Note that with the present data it is only possible to estimate the dissipation rate along the centerline. Nevertheless, the spanwise profiles of the (less suitable) surrogate ε^{iso} indicate that the departures from the centreline value are within 10%, see Fig. 4(d) in Ref. 41.

Of particular importance to the subsequent discussions are the circumferential averages of the terms in Eq. (2) in order to remove the dependence on orientation (\mathbf{r}/r) of the turbulence statistics. The circumferential averages are expected to be good approximations to the averages over spherical shells considering the statistical axisymmetry of the turbulence with respect to the centreline. (Recall that for most of the present data, \mathbf{X} , and therefore r_1 , lies along the centreline. However, for the two datasets acquired off-centreline at $X_2 = y = -6$ mm, one may expect the validity of this assumption to be more doubtful.) The circumferential averages are obtained by integration with respect to the polar angle θ as $\int_0^{\pi/2} A^*(r, \theta, 0) \sin(\theta) d\theta$, where the integrand A^* is any one of the measured terms in Eq. (2) (note that only one quarter of the domain is used due to the reflection symmetry of the structure functions around the r_1 and r_2 axes, the former due to stationarity and the latter by construction). The wind tunnel measurements of Nagata *et al.*⁵ for the decay region in the lee of Fractal Square Grids (FSGs) and the numerical data of Laizet and Vassilicos⁴⁶ for both FSGs and a RG give substantial support to this assumption, and therefore, the circumferential averages are interpreted as spherical shell averages throughout this paper. The spherical shell averaged terms are denoted by removing the superscript asterisk.

B. Anisotropy of energy transfer

The anisotropy of the structure functions $\overline{\delta q^2}(r, \theta, \phi = 0)$ and $\overline{\delta u_i \delta q^2}(r, \theta, \phi = 0)$ is qualitatively investigated from their dependence on θ . (For notational simplicity and due to the assumed axisymmetry, ϕ is not explicitly used as an argument henceforth.) Note that in the present context, anisotropy refers to the dependence of the terms in Eq. (2) on the orientation \mathbf{r}/r (see also Danaïla *et al.*,¹⁰ Lamriben, Cortet, and Moisy⁴⁴) and not to the kinematic relation between the components

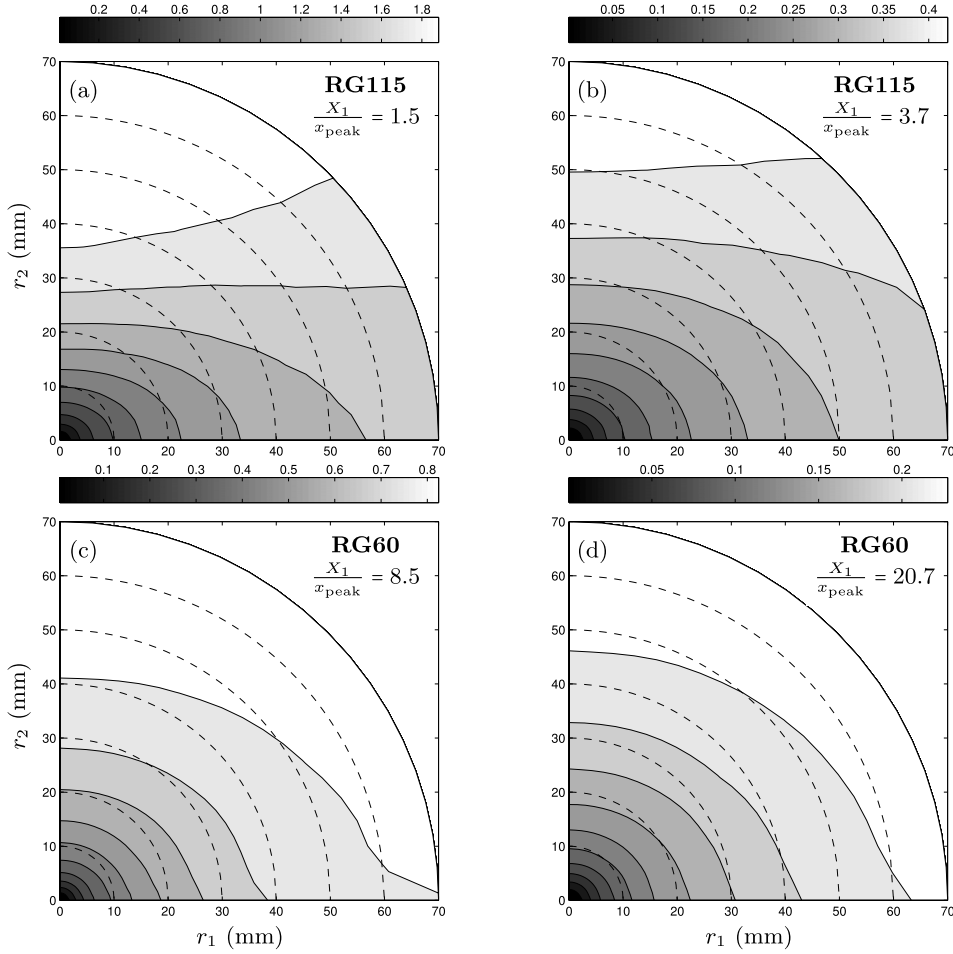


FIG. 5. Iso-contours of the second-order structure functions, $\overline{\delta q^2}(r_1, r_2)$ ($\text{m}^2 \text{s}^{-2}$), at (a), (c) $X_1 = 1250$ mm and (b), (d) $X_1 = 3050$ mm for (top) RG115 and (bottom) RG60 data. $X_1 = 1250$ mm and $X_1 = 3050$ mm correspond to $X_1/x_{\text{peak}} = 1.5$ and $X_1/x_{\text{peak}} = 3.7$ for the RG115 data, and to $X_1/x_{\text{peak}} = 8.5$ and $X_1/x_{\text{peak}} = 20.7$ for the RG60 data. The reference contour levels for isotropic turbulence are added as dashed lines.

of the structure functions parallel and perpendicular to \mathbf{r} (e.g., $\overline{(\delta u_{\parallel})^2}$ versus $\overline{(\delta u_{\perp})^2}$ and $\overline{\delta u_{\parallel}(\delta u_{\parallel})^2}$ versus $\overline{\delta u_{\parallel}(\delta u_{\perp})^2}$), except when clearly indicated. The latter anisotropy considerations are complementary to the first but pertain, for example, to the distribution of kinetic energy between the three orthogonal components and the inter-component energy transfer via pressure fluctuations.^{47,48}

The second-order structure functions $\overline{\delta q^2}(r, \theta)$ are presented in Figs. 5(a)–5(d) for the furthest upstream and downstream measurement locations and for turbulence generated by both RG115 and RG60. Comparing the upstream data (Figs. 5(a) and 5(c)) with the downstream data (Figs. 5(b) and 5(d)) for both grids, there seems to be a tendency for the contours to become increasingly circular as the turbulence decays, i.e., for the energy distribution to become increasingly isotropic. Furthermore, comparing the RG115 with the RG60 data (Figs. 5(a) and 5(b), and 5(c) and 5(d), respectively), it can be seen that the RG115 data, which are acquired closer to the grid in terms of x_{peak} multiples, are less isotropic. Both these observations corroborate a tendency for the kinetic energy to become uniformly distributed over spherical shells for larger x/x_{peak} . Nevertheless, for all cases the small scales seem to remain anisotropic by velocity derivative measures (see Sec. 5 and Tables 4 and 5 of Ref. 41).

Turning to the third-order structure function vectors $\overline{\delta u_i \delta q^2}(r, \theta)$, a similar tendency to isotropy is observed (Figs. 6(a), 6(c) and 7(a), 7(c)). The third-order structure function vectors, which for the RG115 data at $x = 1.5x_{\text{peak}}$ are nearly aligned with the tangential direction (Fig. 6(a)),

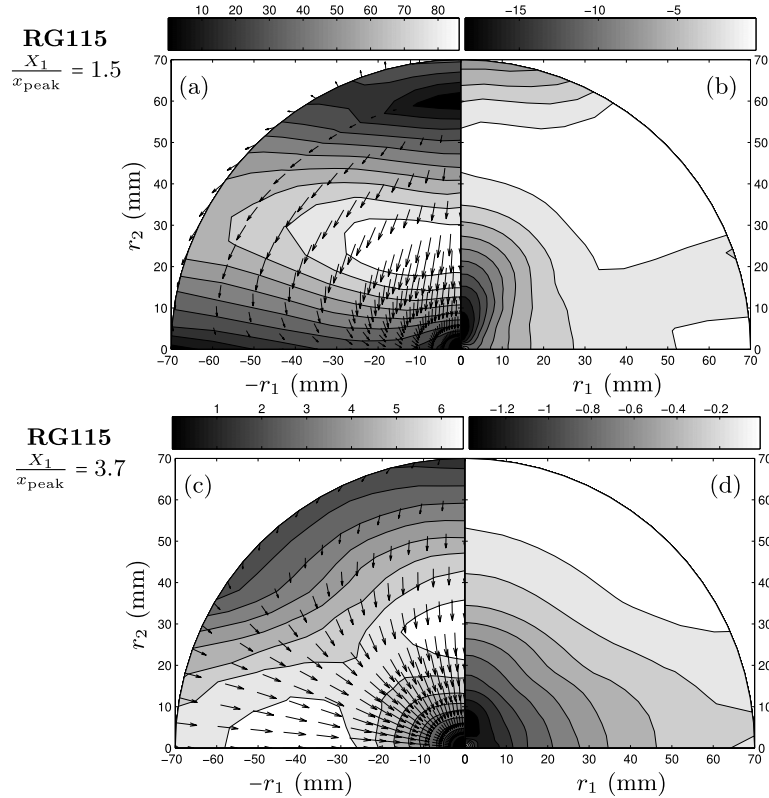


FIG. 6. (a), (c) Third-order structure function vectors, $\overline{\delta u_i \delta q^2}$ and iso-contours of their magnitude, $|\overline{\delta u_i \delta q^2}|$ ($\times 10^{-3} \text{ m}^3 \text{ s}^{-3}$). (b), (d) Iso-contours of the radial contribution of the divergence of $\overline{\delta u_i \delta q^2}$, Π_r^* ($\text{m}^2 \text{ s}^{-3}$). (Top) $X_1 = 1250 \text{ mm}$ and (bottom) $X_1 = 3050 \text{ mm}$. $X_1/x_{\text{peak}} = 1.5$ and $X_1/x_{\text{peak}} = 3.7$ correspond to $X_1 = 1250 \text{ mm}$ and $X_1 = 3050 \text{ mm}$, respectively. Data are acquired in the lee of RG115.

progressively align with the radial direction, and for the RG60 data at $x = 21x_{\text{peak}}$ (Fig. 7(c)) they are indeed nearly so. Note that the divergence of $\overline{\delta u_i \delta q^2}$ (i.e., Π^*) has a radial and a polar contribution (the azimuthal contribution is taken to be zero due to the assumed axisymmetry). As discussed in Sec. I B, the radial contribution Π_r^* (which we plot in Figs. 6(b), 6(d) and 7(b), 7(d)) relates to the interscale energy transfer, whereas the polar contribution Π_θ^* accounts for the redistribution of energy within a spherical shell. The above mentioned tendency to isotropy as the flow decays is very likely linked to the redistribution of energy via Π_θ^* .

IV. THE ROLE OF TURBULENCE PRODUCTION AND TRANSPORT

The effect of transport and production in the single-point kinetic energy balance was investigated in Valente and Vassilicos⁴¹ where it was found that, for the assessed region of the RG115-generated turbulence, both contributions are non-negligible by comparison with the energy dissipation. This region of the RG115-generated turbulence was also compared with an equivalent region of turbulence generated by FSGs and considerable differences were found in the downstream evolution (and transverse profiles) of transport and production relative to the dissipation. Nevertheless, the two different turbulent flows were found to have the same non-classical dissipation behaviour and, consequently, the differences in the production and transport reinforced the view that this non-classical behaviour is present irrespective of the details of the inhomogeneity of the turbulent flow. Indeed, the turbulent transport and production are expected to be large-scale phenomena that play no direct role in the scale-by-scale energy transfer mechanisms, even at these Reynolds numbers ($Re_\lambda = O(100)$). Here, we present data which allow a precise quantification of the effect of production and transport on the scale-by-scale energy budget, Eq. (2).

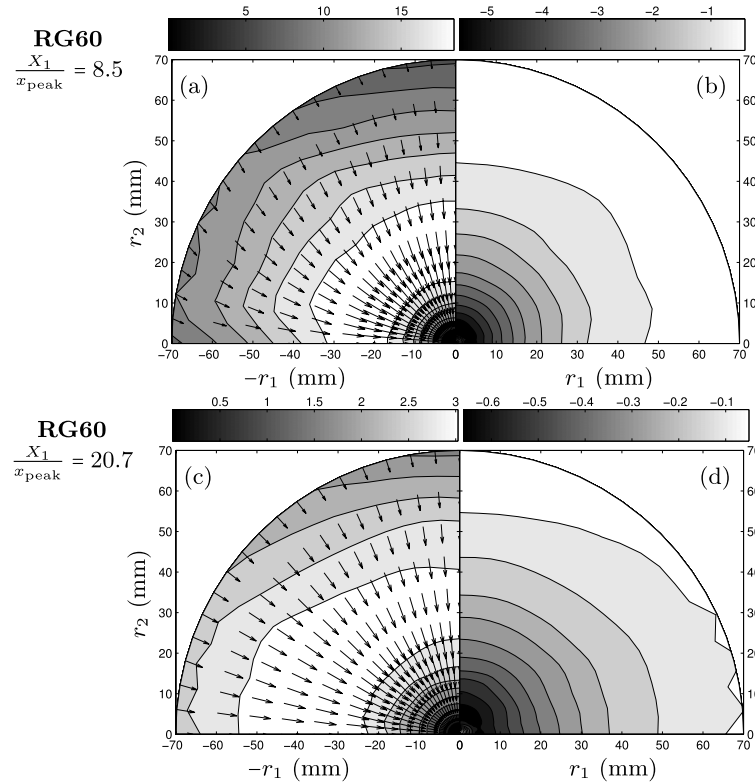


FIG. 7. (a), (c) Third-order structure function vectors, $\overline{\delta u_i \delta q^2}$ and iso-contours of their magnitude, $|\overline{\delta u_i \delta q^2}| (\times 10^{-3} \text{ m}^3 \text{ s}^{-3})$. (b), (d) Iso-contours of the radial contribution of the divergence of $\delta u_i \delta q^2$, Π_r^* ($\text{m}^2 \text{ s}^{-3}$). (Top) $X_1 = 1250 \text{ mm}$ and (bottom) $X_1 = 3050 \text{ mm}$. Data are acquired in the lee of RG60. $X_1/x_{\text{peak}} = 8.5$ and $X_1/x_{\text{peak}} = 20.7$ correspond to $X_1 = 1250 \text{ mm}$ and $X_1 = 3050 \text{ mm}$, respectively.

One may average Eq. (2) over spherical shells to eliminate the dependence of each term on the orientation \mathbf{r}/r yielding the average contribution of each scale to the balance. Retaining all terms except for the linear transfer of energy caused by mean velocity gradients and the scale-by-scale transport by viscous diffusion which were shown to be negligible (see Appendix A), the spherical averaged scale-by-scale energy balance reads

$$\mathcal{A} + \Pi - \mathcal{P} - \mathcal{T} - \mathcal{T}_p = \mathcal{D}_v - \varepsilon, \quad (4)$$

where the \mathcal{T} represents the measured component of turbulent transport and \mathcal{T}_p represents the unknown contribution from the pressure transport.

Turning to the data, the iso-contour maps of the transport and production terms normalised by the dissipation, ε , indicate that most of the transport and production occur at $r \gtrsim L_{11}^{(1)} \approx 30 \text{ mm}$ and $\theta \approx \pi/2$ (Figs. 8(a), 8(c) and 8(b), 8(d)). At smaller values of r , both \mathcal{T} and \mathcal{P} are less than about 15% of ε . Note that the production for large r is much smaller for $\theta \approx 0$ than for $\theta \approx \pi/2$ because $\partial U/\partial y$ tends to zero at the centreline, and the remaining production term, $2\overline{(\delta u)^2} \partial U/\partial x$, is small by comparison. Similarly, the transport for large r and $\theta \approx 0$ is also smaller because the lateral transport overwhelms the longitudinal transport.

The spherical averaged contribution of these terms to balance (4) is plotted together with the spherical shell averaged advection, energy transfer, and viscous diffusion in Figs. 9(a) and 9(b). Note that the dissipation estimates are compensated for the resolution of the sensor, see Sec. 2.2.1 in Ref. 41. The finite resolution of the sensor also biases \mathcal{D}_v since $\lim_{r \rightarrow 0} \mathcal{D}_v(r) = \varepsilon$. A rough compensation for this bias is applied by multiplying \mathcal{D}_v with the ratio between the corrected and the measured ε .

The radial distributions of the advection, energy transfer, and viscous diffusion are similar to those found in the literature for data at comparable Reynolds numbers.²¹ From the data it is

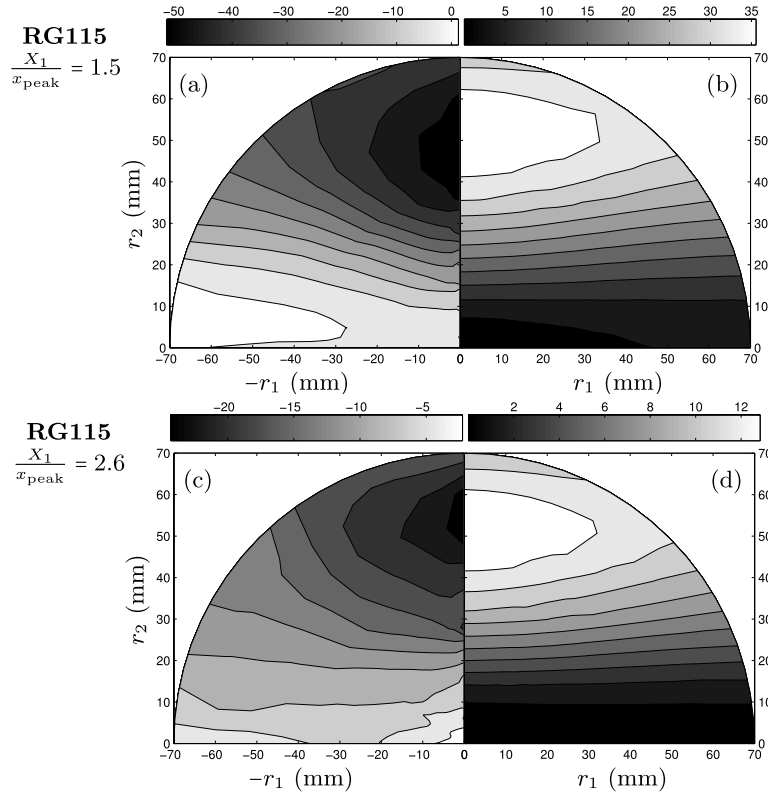


FIG. 8. Normalised turbulence (a), (c) transport, $\mathcal{T}^*/\varepsilon$ (%) and (b), (d) production, $\mathcal{P}^*/\varepsilon$ (%) versus (r_x, r_y) at $x/x_{\text{peak}} = 1.5$ (top) and $x/x_{\text{peak}} = 2.6$ (bottom) in the lee of RG115.

clear that our turbulent transport and production terms are significant for scales of the order of the integral-length scale but become negligible at scales smaller than $r \approx 10 \text{ mm} \approx L_{11}^{(1)}/3$ and therefore cannot tamper with the scale-by-scale energy transfer around its maximum ($r \approx 4 \text{ mm} \approx L_{11}^{(1)}/8$ for the present data). This provides quantitative evidence that the influence of the turbulence production and transport on the energy transfer mechanisms is negligible.

Note that in Figs. 9(a) and 9(b) the balance of the measured terms is also presented. By virtue of (4), the scale-by-scale advection, energy transfer, production, transport, and viscous diffusion should balance the dissipation plus the unknown contribution from scale-by-scale pressure transport, \mathcal{T}_p . Even though \mathcal{T}_p is not accounted for, it can be seen that there is a reasonable balance between the measured terms, at least within the expected uncertainty of the data. Note that the error bars added to the balance ($\mathcal{D}_v + \mathcal{P} + \mathcal{T} - \Pi - \mathcal{A}$, see Figs. 9(a) and 9(b)) underestimate the overall uncertainty of the data since they do not take into account uncertainties associated with the measurements of the advection, transport, and production terms and possible departures from the assumptions used to compute the terms in Eq. (2), see Sec. III A.

V. ADVECTION, ENERGY TRANSFER, AND DISSIPATION SCALINGS

We now investigate how the stark differences in the way the energy dissipation scales in the two decay regions identified in Ref. 12 downstream of a turbulence-generating grid relate to the advection, energy transfer, and viscous diffusion during decay (the remaining terms in Eq. (4) are negligible at small enough values of r as shown in Fig. 9).

Starting with the RG60 data, the evolution in the further downstream decay region between $x = 8.5x_{\text{peak}}$ and $x = 21x_{\text{peak}}$ of the scale-by-scale viscous diffusion, downscale energy transfer, and advection normalised by the dissipation is shown in Fig. 10(a). As the turbulence decays the relative

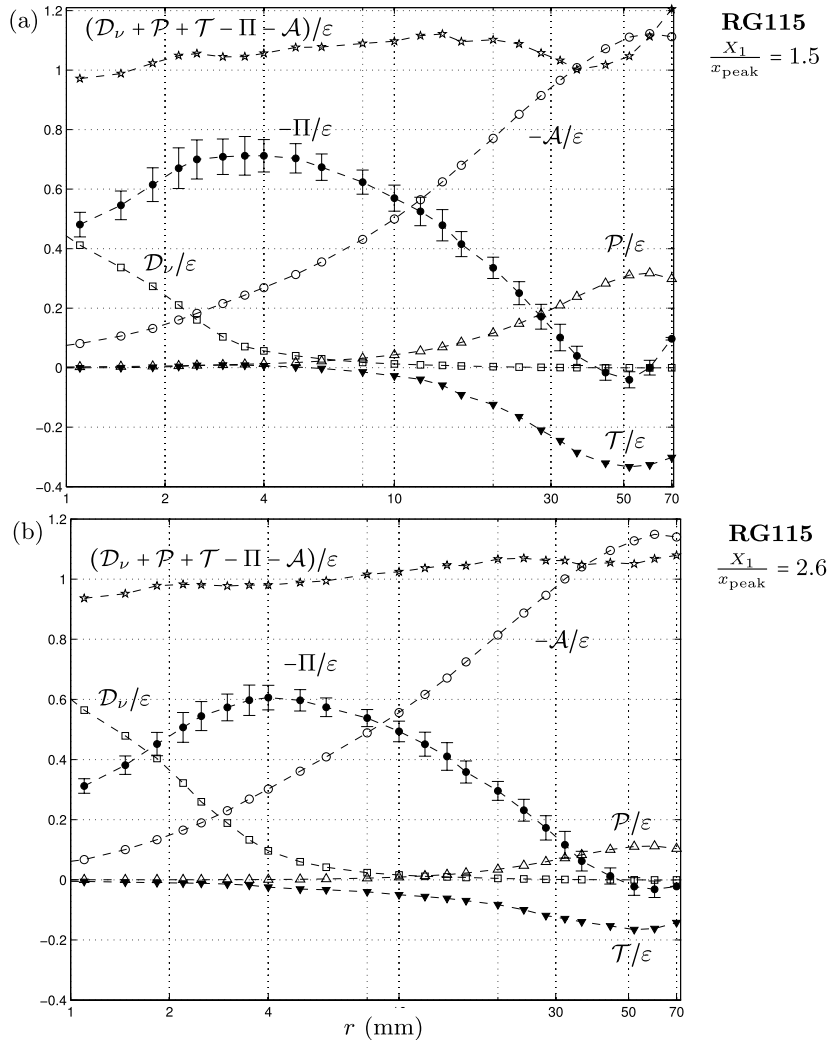


FIG. 9. Spherically averaged (filled circle) $-\Pi/\varepsilon$, (open circle) $-\mathcal{A}/\varepsilon$, (open square) $\mathcal{D}_\nu/\varepsilon$, (open triangle) \mathcal{P}/ε , (filled down triangle) \mathcal{T}/ε , and (open star) $(\mathcal{D}_\nu + \mathcal{P} + \mathcal{T} - \Pi - \mathcal{A})/\varepsilon$ at (a) $x/x_{\text{peak}} = 1.5$ and (b) $x/x_{\text{peak}} = 2.6$ for RG115-generated turbulence, showing that turbulence production and transport are small for scales around the maximum energy transfer Π . The 95% confidence intervals of Π/ε (see Sec. II B) are represented in the figures.

importance of the various terms in the balance is retained and most of the spread appears in the form of a move to higher length-scales (in mm) as the downstream location of X_1 increases (see arrow in Fig. 10(a)). As shown in Fig. 10(b), this move is in fact due to the increase in turbulent scales with increasing X_1 . The scaling of the abscissae is, however, secondary to the main discussion here which pertains to the relative magnitude of the advection, the energy transfer, the viscous diffusion, and the dissipation. Note that the viscous diffusion is very small compared to the dissipation at scales $r \geq \lambda$ for both our RG60 data (see Fig. 10(b)) and our RG115 data (Fig. 11(b)), in agreement with a mathematical proof of this fact which we give in Appendix B. Of particular importance in Fig. 10(b) is the observation that the maximum absolute value of the energy transfer $\Pi|_{\text{max}}$ is roughly a constant fraction of the dissipation throughout the downstream extent of the data corresponding to a range of local Reynolds numbers Re_λ between 100 and 80 ($-\Pi|_{\text{max}} \approx 0.55\varepsilon$ with the peak located at $r \approx \lambda$, see Fig. 10(b)).

In fact, taking the numerical values of $\Pi|_{\text{max}}$ and the numerical values of the advection at the separation r^* where $\Pi(r^*) = \Pi|_{\text{max}}$ and normalising the data with $(\bar{u}^2)^{3/2}/L_{11}^{(1)}$, it is clear from Fig. 13(a) that $-\mathcal{A}|_{\text{max}}(\Pi)L_{11}^{(1)}/(\bar{u}^2)^{3/2} \sim C_\Pi^{(1)} \sim C_\varepsilon^{(1)} \approx \text{constant}$ (where $C_\varepsilon^{(1)} \equiv \varepsilon L_{11}^{(1)}/(\bar{u}^2)^{3/2}$,

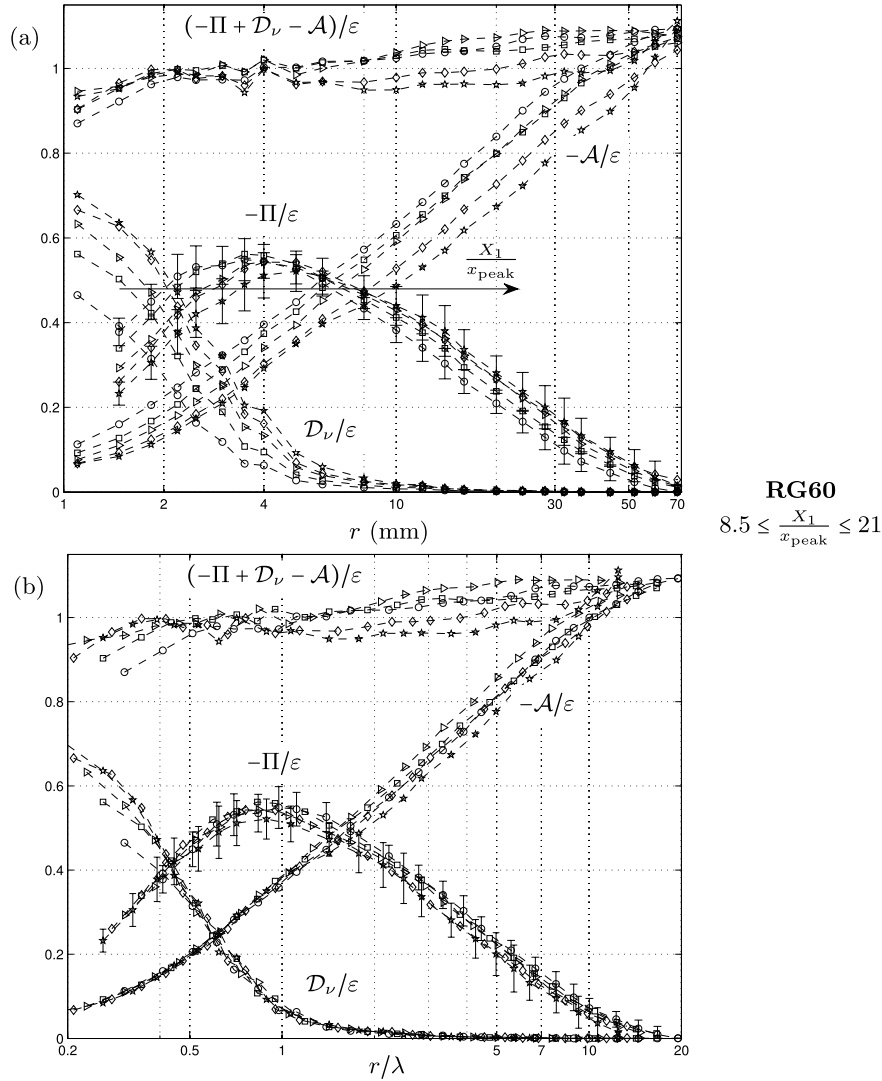


FIG. 10. Normalised, spherical shell averaged scale-by-scale energy transfer ($-\Pi/\varepsilon$), advection ($-\mathcal{A}/\varepsilon$), and viscous diffusion ($\mathcal{D}_\nu/\varepsilon$) versus (a) r and (b) r/λ during the decay of turbulence generated by RG60 at (open circle) $x/x_{\text{peak}} = 8.5$, (open square) $x/x_{\text{peak}} = 11.5$, (open triangle right) $x/x_{\text{peak}} = 16.6$, (diamond) $x/x_{\text{peak}} = 17.6$, and (open star) $x/x_{\text{peak}} = 21$. The 95% confidence intervals of Π/ε (see Sec. II B) are added to the furthestmost up- and downstream locations. The arrow in the upper figure indicates the direction in which the viscous diffusion, energy transfer, and advection curves move as X_1 increases.

$C_{\Pi}^{1(1)} \equiv -\Pi|_{\text{max}} L_{11}^{(1)} / (\overline{u^2})^{3/2}$, and $L_{11}^{(1)}$ is the usual longitudinal integral length-scale). The viscous diffusion term, $\mathcal{D}_\nu|_{\text{max}(\Pi)}$ is smaller than any of the other terms at this moderate Re_λ ($< 10\%$ of the dissipation) and it is difficult to discern whether $\mathcal{D}_\nu|_{\text{max}(\Pi)}$ is constant or decreases with increasing Re_λ as one might expect.

Turning to the RG115 data presented in Fig. 11(a), two outstanding differences in the downstream evolution of these quantities can be registered: (i) the peak value of the energy transfer does not scale with the dissipation and (ii) the curves representing the advection seem to move slightly to smaller length scales (in mm) as X_1 increases in the opposite direction than was the case for the RG60 data (Fig. 10(a)). Normalising the abscissae with λ takes into account most of the changes in the viscous diffusion term but now augments the move of the advection term to lower length-scales as X_1 increases (see Fig. 11(b) and compare with Fig. 10(b)). (Note that for the RG115 data in this region, $L_{11}^{(1)}/\lambda \sim \text{constant}$ as shown in Ref. 12, hence the normalisation of the abscissae with $L_{11}^{(1)}$

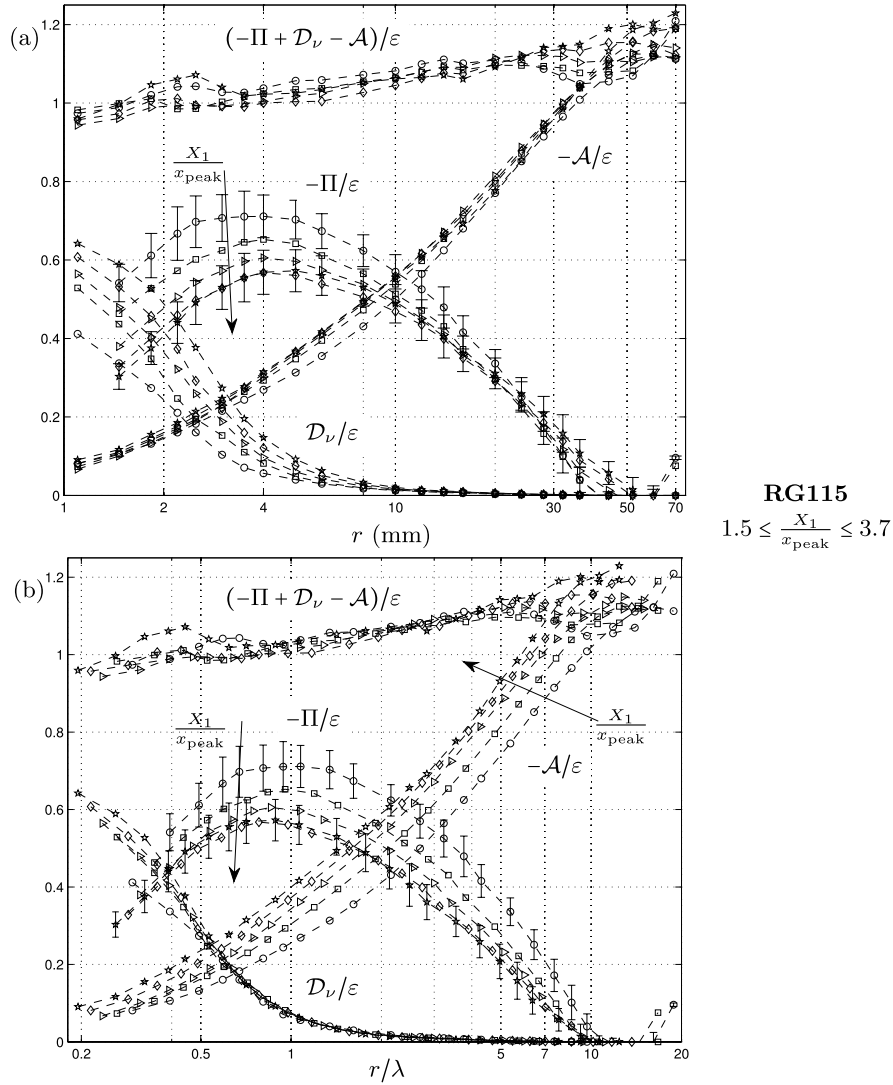


FIG. 11. Normalised, spherical shell averaged scale-by-scale energy transfer $(-\Pi/\varepsilon)$, advection $(-A/\varepsilon)$, and viscous diffusion (D_ν/ε) versus (a) r and (b) r/λ during the decay of turbulence generated by RG115 at (open circle) $x/x_{\text{peak}} = 1.5$, (open square) $x/x_{\text{peak}} = 2.0$, (open triangle right) $x/x_{\text{peak}} = 2.6$, (diamond) $x/x_{\text{peak}} = 3.1$ and (open star) $x/x_{\text{peak}} = 3.7$. The 95% confidence intervals of Π/ε (see Sec. II B) are added to the furthestmost up- and downstream locations. The arrow in the upper figure indicates the direction in which the energy transfer curves move as X_1 increases and the arrows in the lower figure indicate the directions in which the energy transfer and the advection curves move as X_1 increases.

would yield an identical horizontal collapse as that presented in Fig. 11(b).) Concerning the scaling of the ordinates, it should be noted that, if instead of ε one chooses to normalise the ordinates by $(\overline{u^2})^{3/2}/L_{11}^{(1)}$ (Fig. 12), the vertical spread of the energy transfer data is much reduced, but the spread of the advection is further augmented (as is the spread of the viscous diffusion term, since in the limit $r \rightarrow 0$ this term is equal to the dissipation and, as shown in Ref. 12, ε does not scale with $(\overline{u^2})^{3/2}/L_{11}^{(1)}$ in this region).

The procedure of normalising ε , $\Pi|_{\text{max}}$, $A|_{\text{max}(\Pi)}$, and $D_\nu|_{\text{max}(\Pi)}$ with $(\overline{u^2})^{3/2}/L_{11}^{(1)}$ is repeated, and the data are plotted in Fig. 13(b) against Re_λ . Even though the dissipation follows $C_\varepsilon^{1(1)} = f(Re_M)/Re_\lambda$ in this region, it is clear that the behaviour of $C_\Pi^{1(1)}$ is strikingly different. In fact, $C_\Pi^{1(1)}$ is approximately constant and with the same numerical value ($C_\Pi^{1(1)} \approx 0.6$) as the one that we find for the RG60 data in the further downstream region (in multiples of x_{peak}) where $C_\varepsilon^{1(1)}$ is approximately

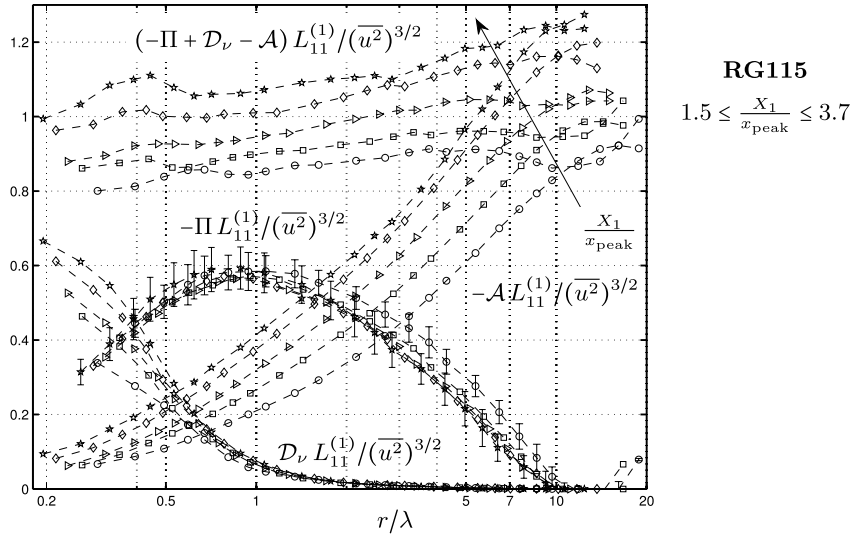


FIG. 12. Normalised, spherical shell averaged scale-by-scale energy transfer $(-\Pi L_{11}^{(1)}/(\overline{u^2})^{3/2})$, advection $(-A L_{11}^{(1)}/(\overline{u^2})^{3/2})$, and viscous diffusion $(D_\nu L_{11}^{(1)}/(\overline{u^2})^{3/2})$ versus r/λ during the decay of turbulence generated by RG115 at (open circle) $x/x_{\text{peak}} = 1.5$, (open square) $x/x_{\text{peak}} = 2.0$, (open triangle right) $x/x_{\text{peak}} = 2.6$, (diamond) $x/x_{\text{peak}} = 3.1$, and (open star) $x/x_{\text{peak}} = 3.7$. The 95% confidence intervals of Π/ε (see Sec. II B) are added to the furthestmost up- and downstream locations. The arrow indicates the direction in which the advection curve moves as X_1 increases.

constant. Note also that the normalised advection term grows faster than Re_λ^{-1} with decreasing Re_λ and therefore adapts to cover most of the growing difference between the constant $C_\Pi^{(1)}$ and the increasing $C_\varepsilon^{(1)}$ as the flow decays and Re_λ decreases. The different Reynolds number scalings of C_Π and C_ε are intrinsically different and will of course remain different if a length-scale different from an integral length-scale is used to non-dimensionalise dissipation and maximum energy transfer.⁴⁹ The viscous diffusion term $D_\nu|_{\text{max}(\Pi)}$ is also small for the present data, similar to what is found for the RG60 data.

A. Discussion

The present work is concerned with the validity of the energy transfer/dissipation balance over a range of length-scales r , i.e.,

$$\Pi(\mathbf{X}, r) = \Pi|_{\text{max}}(\mathbf{X}) = -\varepsilon(\mathbf{X}), \quad (5)$$

where instead of using (local) isotropy, $\Pi^*(\mathbf{X}, r)$ is averaged over spherical shells.¹⁶ Note that we have approximated our flow as being locally homogeneous to remove the dependence of the right-hand-side on the separation r . We do so based on our RG115 data where $\text{max}(\Pi)$ is located at $r \simeq 5$ mm, cf. Fig. 11(a), corresponding to $y/M \simeq \pm 0.02$; for such close locations, no appreciable changes in the dissipation rate can be observed, see Fig. 4(d) in Ref. 41. Finally, note also that $\Pi|_{\text{max}}$ in physical space is equal to its wavenumber space counterpart, see Appendix C.

It is clear from the outset that the Reynolds numbers of the present data are insufficiently high to allow verification of Eq. (5) over a range of length-scales r . What the present data do allow us to report for the first time, however, is that $\Pi|_{\text{max}} \sim (\overline{u^2})^{3/2}/L_{11}^{(1)}$ both in far downstream turbulence where $C_\varepsilon^{(1)} \approx \text{constant}$ and in non-equilibrium turbulence where $C_\varepsilon^{(1)} = f(Re_M)/Re_\lambda$ and Re_λ is higher (see Figs. 13(a) and 13(b); see also Refs. 8 and 50). In this non-equilibrium region, our data also demonstrate the growing importance of the small-scale advection with increasing streamwise distance from the grid. This increasing importance is directly linked to the growing imbalance between $\Pi|_{\text{max}}$ and ε (see Fig. 13(b) and recall that Re_λ decreases with increasing streamwise distance in the decay region downstream of the turbulence-generating grid). This growing imbalance

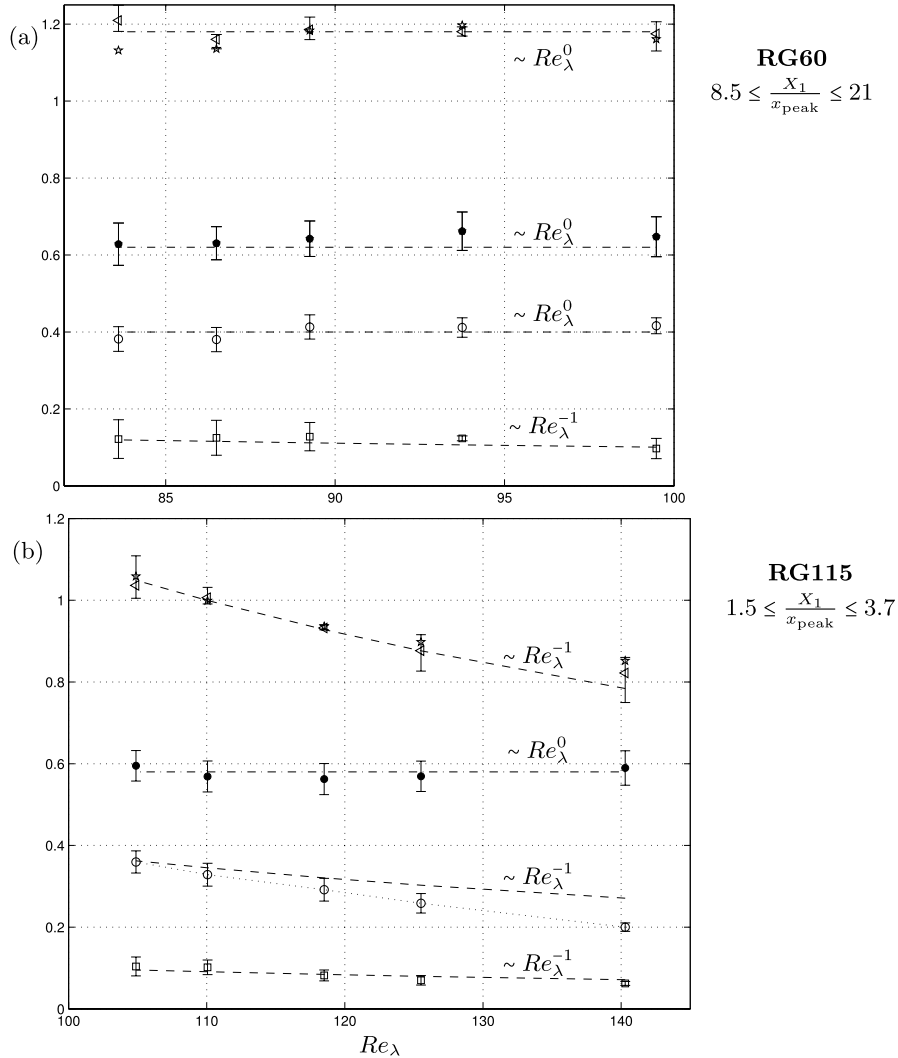


FIG. 13. Normalised energy dissipation, maximum scale-by-scale energy transfer and scale-by-scale advection, and viscous diffusion at the maximum energy transfer versus Re_λ showing the stark difference in behaviour throughout (a) the far downstream region at the lee of RG60 and (b) the non-equilibrium region at the lee of RG115; (open triangle left) $C_\varepsilon^{1(1)}$, (filled circle) $C_\Pi^{1(1)} \equiv -\Pi|_{\max} L_{11}^{(1)}/(\overline{u^2})^{3/2}$, (open circle) $-\mathcal{A}|_{\max(\Pi)} L_{11}^{(1)}/(\overline{u^2})^{3/2}$, (open square) $\mathcal{D}_v|_{\max(\Pi)} L_{11}^{(1)}/(\overline{u^2})^{3/2}$, and (open star) $(\mathcal{D}_v|_{\max(\Pi)} - \Pi|_{\max} - \mathcal{A}|_{\max(\Pi)}) L_{11}^{(1)}/(\overline{u^2})^{3/2}$. Dashed and dashed-dotted lines follow $\sim Re_\lambda^{-1}$ and $\sim Re_\lambda^0$, respectively, as indicated in the figures.

with streamwise distance eventually stops growing when the $C_\varepsilon^{1(1)} = \text{constant}$ region starts. In that region, dissipation ε , maximum transfer $\Pi|_{\max}$, and small-scale advection $\mathcal{A}|_{\max(\Pi)}$ (see Fig. 13) are all three proportional to $(\overline{u^2})^{3/2}/L_{11}^{(1)}$ and therefore decay together. Note that turbulence in this $C_\varepsilon^{1(1)} = \text{constant}$ region is not in Richardson-Kolmogorov equilibrium which would have required the small-scale advection to be negligible compared to dissipation and transfer. It might of course be that the Reynolds numbers at our measuring stations are not high enough for this. But the small-scale advection grows in magnitude relative to dissipation throughout the non-equilibrium region and then reaches a plateau in the $C_\varepsilon^{1(1)} = \text{constant}$ region. There are essentially only two different ways (and their combinations) in which this behaviour can be a FRN effect: either (i) the non-equilibrium region shrinks in streamwise extent as the inlet Reynolds number increases while, at the same time, the small-scale advection becomes progressively smaller throughout the field; or (ii) the small-scale advection becomes smaller throughout the field as the inlet Reynolds number

increases without a modification in the streamwise extent of the non-equilibrium region but with a modification of the Reynolds number scalings of dissipation and interscale transfer. Only future experiments at higher Reynolds numbers will be able to settle this question.^{8,21,28}

Even though the constancy of $C_\varepsilon^{(1)}$ is usually expected as a high Reynolds number asymptotic, the $C_\varepsilon^{(1)}$ constancy appears at distances much further downstream in our experiments where the local Reynolds number has in fact further decayed (though, clearly, not enough for $C_\varepsilon^{(1)}$ not to be constant as a result of the local Reynolds number being too low). The constancy of $C_\varepsilon^{(1)}$ in this far downstream region appears in our RG60 experiments with a rate of change of the local Reynolds number which is enough for $C_\varepsilon^{(1)}$ to vary in proportion to $1/Re_\lambda$ in the non-equilibrium region (compare Figs. 13(a) and 13(b)). Note the high value of the constant $C_\varepsilon^{(1)}$ in the RG60 decay region experiment (Fig. 13(a)), high by comparison to values of this constant recorded for forced statistically stationary turbulence, and in agreement with different spectral imbalance arguments.^{8,35} Note that this is a region where there is a “balance” between the scalings of $\Pi|_{\max}$ and ε (i.e., they both scale as $(\overline{u^2})^{3/2}/L_{11}^{(1)}$) whereas such a scaling balance is absent in what we term the non-equilibrium decay region.

Finally, we note that similar findings were recently reported in decaying homogeneous isotropic DNSs.^{8,9} This reinforces our conclusion that the present behaviour is manifested in spite of the turbulence being inhomogeneous and anisotropic. It also shows the ability of our approach to obtain reasonable estimates of the energy cascade flux even in inhomogeneous and anisotropic turbulence, the former by confirming its negligible effect at small-scales and the latter by averaging over spherical shells. This motivates similar investigations in other turbulent flows where the behaviour of the energy cascade remains poorly understood, such as in jets and wakes.

VI. CONCLUSION

An experimental investigation of the downstream evolution of the scale-by-scale energy transfer budget for both the non-equilibrium ($C_\varepsilon \sim f(Re_M)/Re_\lambda$) and the further downstream $C_\varepsilon \approx$ constant decay regions of regular grid-generated turbulence at Reynolds numbers Re_λ below 150 is presented.

We have shown that the turbulent production and transport are large-scale effects which are negligible at length-scales smaller than $\ell/3$ even though our Reynolds numbers are moderate (ℓ is an integral length-scale taken, here, to be the longitudinal integral length-scale $L_{11}^{(1)}$). Hence, production and transport do not influence the maximum energy transfer to smaller-scales. However, since the flow is anisotropic, reliable estimates of the non-linear energy transfer rate require the two-point/two-components measurements which we present here for the first time, rather than the usual assessment of the longitudinal third-order structure functions.¹¹

We find that the maximum energy transfer rate $\Pi|_{\max}$ scales as $(\overline{u^2})^{3/2}/L_{11}^{(1)}$ both in the turbulence decay region which we term non-equilibrium region and in the further downstream turbulence decay region where $C_\varepsilon \approx$ constant. This is a noteworthy finding which could not be anticipated by any of the previous experimental works since it implies that the scalings of $\Pi|_{\max}$ and ε are different in the non-equilibrium region. These different scalings and the related imbalance between $\Pi|_{\max}$ and ε in the non-equilibrium region are consistent with the presence of non-negligible small-scale advection and the increase of this small-scale advection in proportion to the maximum energy transfer as the turbulence decays. Further downstream where the turbulence decay enters its $C_\varepsilon \approx$ constant region, the small-scale advection remains about constant in proportion to the maximum energy transfer, presumably until the Reynolds number drops to levels so low that viscosity becomes dominant. It is also a noteworthy and perhaps unexpected finding that $C_\varepsilon \approx$ constant coexists with significant small-scale advection in the further downstream region where it appears.

Note that neither the turbulence in the non-equilibrium nor the $C_\varepsilon \approx$ constant regions of our flows are in Richardson-Kolmogorov equilibrium (which would imply $\Pi|_{\max} = \varepsilon$). Departures from the Richardson-Kolmogorov equilibrium are usually attributed to finite Reynolds number effects,^{21,28} but they could also be caused by different types of spectral imbalances which may persist in some form at high Reynolds numbers.^{8,30–32} In fact recent DNS of non-equilibrium periodic

turbulence⁹ suggests that the departure becomes even more pronounced, in fact qualitatively so, at Reynolds numbers up to about an order of magnitude higher than the ones accessible in the present wind tunnel experiment.

Finally, it should be stressed that the best defined power-law energy spectra with exponents closest to $-5/3$ in the grid-generated decaying turbulence have been recorded in the non-equilibrium region¹² where, irrespective of the fact that $-5/3$ is the Kolmogorov exponent, the lack of balance even in scaling terms between interscale transfer and dissipation indicates a clear non-Richardson-Kolmogorov cascade.^{2,40} It is important to know that non-equilibrium cascades such as the ones in the lee of various grid-generated turbulent flows can follow well-defined scaling laws such as the one for dissipation studied in detail in Ref. 41 and the one for maximum interscale energy transfer established here at moderate Reynolds numbers.

ACKNOWLEDGMENTS

This work was carried out at Imperial as part of Pedro Valente's Ph.D. programme with the financial support from Fundação para a Ciência e a Tecnologia (SFRH/BD/61223/2009, cofinanced by POPH/FSE). We are grateful to Professor Arne Johansson (KTH) for the discussion concerning the experimental apparatus. P.C.V. would like to thank Dr. Anthony R. Oxlade for the help in the digital imaging system setup, and Ian Pardew and Roland Hutchins (aero-workshop) for the manufacture of the apparatus.

APPENDIX A: ESTIMATES OF Π_U^* AND $\mathcal{D}_{X,\nu}^*$

The energy transfer due to mean velocity gradients, Π_U^* , and the transport via viscous diffusion, $\mathcal{D}_{X,\nu}^*$, are shown to be negligible compared to the other terms in Eq. (2). These terms are computed from the acquired data as described in Sec. III A. As shown in Fig. 14, the term Π_U^* averaged over spherical shells represents less than 0.4% of the dissipation at $X_1/x_{\text{peak}} = 1.5$ and further downstream, $X_1/x_{\text{peak}} = 2.6$, it decreases to less than 0.05%. The transport via viscous diffusion averaged over spherical shells, $\mathcal{D}_{X,\nu}$ is also negligible and represents less than 0.1% for both downstream locations, $X_1/x_{\text{peak}} = 1.5$ and $X_1/x_{\text{peak}} = 2.6$ (see Fig. 14).

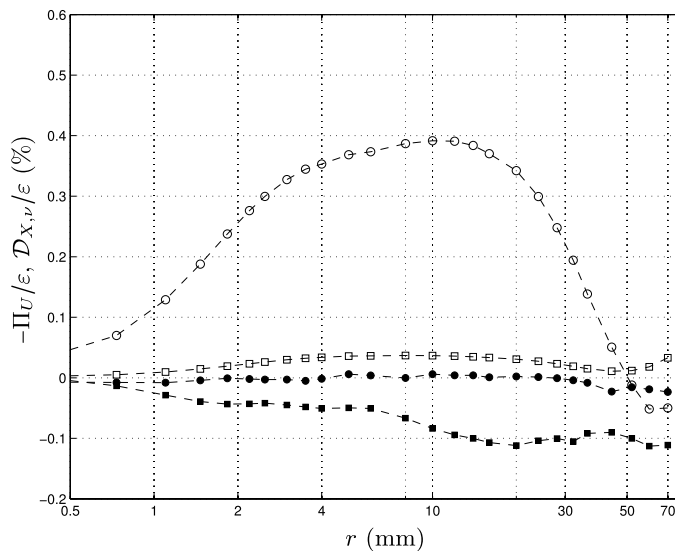


FIG. 14. Negligible terms in (2) averaged over spherical shells and normalised by the dissipation. (Open circle | open square) $-\Pi_U/\varepsilon$ (%) at $X_1 = 1250$ mm and $X_1 = 2150$ mm, respectively, and (filled circle | filled square) $\mathcal{D}_{X,\nu}/\varepsilon$ (%) at $X_1 = 1250$ mm and $X_1 = 2150$ mm, respectively. $X_1 = 1250$ mm and $X_1 = 2150$ mm correspond to $X_1/x_{\text{peak}} = 1.5$ and $X_1/x_{\text{peak}} = 2.6$, respectively. Data are acquired in the lee of RG115.

APPENDIX B: A KINEMATIC UPPER BOUND FOR THE SCALE-BY-SCALE VISCOUS DIFFUSION

Under very plausible assumptions on the functional form of

$$S_2(\mathbf{X}, \mathbf{r}) = \frac{1}{4\pi} \int d\Omega \overline{\delta q^2}(\mathbf{X}, \mathbf{r})$$

(the second-order structure function averaged over all directions \mathbf{r}/r where Ω is the solid angle), we show that the spherical averaged viscous diffusion term appearing in Eq. (2) has an upper bound of the form

$$\begin{aligned} \mathcal{D}_\nu(\mathbf{X}, r) &\equiv \frac{\nu}{2} \frac{\partial^2 S_2(\mathbf{X}, r)}{\partial r_k^2} < \\ &\frac{4\nu}{r^2} S_2(\mathbf{X}, r) < \frac{4\nu}{r^2} 4K^*(\mathbf{X}, r) \quad \forall r, \end{aligned} \quad (\text{B1})$$

where $4K^*(\mathbf{X}, r)$ is the sum of twice the turbulent kinetic energy at the two locations, $\mathbf{X} - \mathbf{r}/2$ and $\mathbf{X} + \mathbf{r}/2$.

This inequality is useful in determining upper ranges of r where $\mathcal{D}_\nu(\mathbf{X}, r)$ is negligible by comparison to some other term in (2). Considering, for example, the dissipation term $4\varepsilon^*(\mathbf{X}, r)$ in (2), this inequality can be used to show that if $\frac{4\nu}{r^2} 4K^*(\mathbf{X}, r) \ll 4\varepsilon^*(\mathbf{X}, r)$, then $\mathcal{D}_\nu(\mathbf{X}, r) \ll 4\varepsilon^*(\mathbf{X}, r)$. In other words, the spherical averaged viscous term \mathcal{D}_ν is negligible compared to $4\varepsilon^*$ in the upper range of scales $r \gg \lambda^*$, where $\lambda^* \equiv \sqrt{4\nu K^*/\varepsilon^*}$. Clearly λ^* is close to a fraction of the Taylor microscale λ , in fact close to $\sqrt{2/5}\lambda$, where turbulent kinetic energy gradients and turbulent dissipation gradients are small and this is indeed the case in the flow regions where the results reported in Sec. V are observed. One of these results is that \mathcal{D}_ν is small compared to $4\varepsilon^*$ for $r > \lambda$ (see Figs. 10(b) and 11(b)), a result which can therefore be considered to be a simple kinematic consequence of the inequality established in this appendix. This conclusion and (B1) in general are generalisations in physical space of similar results previously obtained in Fourier space for homogeneous turbulence by a very different method.⁵¹

We now proceed by proving inequalities (B1).

We start by writing the Laplacian of $S_2(\mathbf{X}, r)$ in spherical coordinates,

$$\begin{aligned} \frac{\partial^2 S_2(\mathbf{X}, r)}{\partial r_k^2} &= r^{-2} \frac{\partial}{\partial r} \left(r^2 \frac{\partial S_2(\mathbf{X}, r)}{\partial r} \right) \\ &= \frac{\partial^2 S_2(\mathbf{X}, r)}{\partial r^2} + \frac{2}{r} \frac{\partial S_2(\mathbf{X}, r)}{\partial r} \end{aligned}$$

and noting that

$$\lim_{r \rightarrow 0} \frac{\partial^2 S_2(\mathbf{X}, r)}{\partial r_k^2} = 3 \lim_{r \rightarrow 0} \frac{\partial^2 S_2(\mathbf{X}, r)}{\partial r^2} = \varepsilon(\mathbf{X})/\nu.$$

Taylor expanding about $r = 0$ implies that $S_2(\mathbf{X}, r) = 3\varepsilon(\mathbf{X})/(2\nu)r^2$ for small enough values of r . At large enough values of r , $S_2(\mathbf{X}, r) \approx 4K^*(\mathbf{X}, r)$; more accurately, $\lim_{r \rightarrow \infty} S_2(\mathbf{X}, r) = 4K^*(\mathbf{X}, r)$.

We assume (i) that S_2 is a monotonically increasing function in $0 \leq r < \infty$ with continuous first- and second-order derivatives with respect to r ; (ii) that it has only one inflection point at $r = r_I$, i.e., $\frac{\partial^2 S_2(\mathbf{X}, r)}{\partial r^2}(r) = 0$ only at $r = r_I$; and (iii) that $\frac{\partial S_2(\mathbf{X}, r)}{\partial r}(r)$ is concave in the range $0 \leq r \leq r_I$. The monotonicity assumption directly implies that $S_2 < 4K^*$ which deals with the second inequality in (B1).

The existence of an inflection point is consistent with the commonly observed functional form of $S_2(r)$, where $S_2(\mathbf{X}, r) \sim r^2$ for small r followed by a smooth transition to a power-law of the type $S_2(\mathbf{X}, r) \sim r^n$ with $n < 1$ ($n = 2/3$ for Kolmogorov's inertial range). The inflection point resides at a value of r between these two power laws. The absence of another inflection point agrees with the monotonically increasing passage from the $n < 1$ power law to a constant (independent of r).

The assumption that $\frac{\partial S_2(\mathbf{X}, r)}{\partial r}(r)$ is concave in the range $0 \leq r \leq r_I$ and then monotonically decreasing at $r > r_I$ is enough to establish that

$$S_2(\mathbf{X}, r) = \int_0^r \frac{\partial S_2(\mathbf{X}, \zeta)}{\partial \zeta} d\zeta > \frac{r}{2} \frac{\partial S_2(\mathbf{X}, r)}{\partial r} \quad \forall r. \quad (\text{B2})$$

This can be seen as a geometrical inequality relating the area of the triangle of base r and height $\partial S_2(\mathbf{X}, r)/\partial r$ with the area underneath $\partial S_2(\mathbf{X}, \zeta)/\partial \zeta$ for $0 \leq \zeta \leq r$. By a similar geometric reasoning for $r \leq r_I$,

$$\frac{\partial S_2(\mathbf{X}, r)}{\partial r} = \int_0^r \frac{\partial^2 S_2(\mathbf{X}, \zeta)}{\partial \zeta^2} d\zeta > \frac{r}{2} \frac{\partial^2 S_2(\mathbf{X}, r)}{\partial r^2} \quad \forall r \leq r_I, \quad (\text{B3})$$

which combined with (B2) leads to

$$\begin{aligned} r^{-2} \frac{\partial}{\partial r} \left(r^2 \frac{\partial S_2(\mathbf{X}, r)}{\partial r} \right) &= \frac{\partial^2 S_2(\mathbf{X}, r)}{\partial r^2} + \\ &\frac{2}{r} \frac{\partial S_2(\mathbf{X}, r)}{\partial r} < \frac{8 S_2(\mathbf{X}, r)}{r^2} \quad \forall r \leq r_I. \end{aligned} \quad (\text{B4})$$

For $r > r_I$, $\partial^2 S_2(\mathbf{X}, r)/\partial r^2 < 0$, and $\partial S_2(\mathbf{X}, r)/\partial r > 0$ by assumption, thus

$$\frac{\alpha}{r} \frac{\partial S_2(\mathbf{X}, r)}{\partial r} > \frac{\partial^2 S_2(\mathbf{X}, r)}{\partial r^2} \quad \forall \alpha \geq 0, \quad (\text{B5})$$

which together with (B2) leads to

$$r^{-2} \frac{\partial}{\partial r} \left(r^2 \frac{\partial S_2(\mathbf{X}, r)}{\partial r} \right) < \frac{2(2 + \alpha) S_2(\mathbf{X}, r)}{r^2} \quad \forall \alpha \geq 0, \quad \forall r \geq r_I. \quad (\text{B6})$$

Inequalities (B4) and (B6) (with $\alpha = 2$ for convenience) can now be combined to yield the first inequality in (B1).

APPENDIX C: EQUALITY OF $\Pi|_{\max}$ IN PHYSICAL AND WAVENUMBER SPACE

We note that the maximum nonlinear energy transfer in physical space, $\Pi|_{\max}$, is equal to its wavenumber space counterpart, $\Pi_K|_{\max} = \Pi|_{\max} (\Pi_K \equiv \int_0^K T(k) dk)$, where $T(k)$ is the spherical averaged non-linear spectral transfer term, see, e.g., Ref. 20). This can be seen from Eq. (6.17) of Frisch,²⁰ noting that $\nabla_\ell \cdot (\ell/\ell^2 \Pi(\ell))|_{\Pi(\ell)=\Pi|_{\max}} = \Pi|_{\max}/\ell^2$ and that $\int_{\mathbb{R}^3} d^3\ell \sin(K\ell)/\ell^3 = 2\pi^2$ (using the book's notation and defining $\Pi(\ell) \equiv \nabla_\ell \cdot \langle |\delta \mathbf{u}(\ell)|^2 \delta \mathbf{u}(\ell) \rangle / 4$ and $\Pi|_{\max} \equiv \max(|\Pi(\ell)|)$). For an inhomogeneous turbulent flow, care must be taken in guaranteeing existence of the Fourier transform.^{37,39} Contrastingly, it is not straightforward to establish a simple relationship between $\overline{\delta u_\parallel \delta q^2}/r$ or $(\overline{\delta u_\parallel})^3/r$ and a wavenumber space counterpart, see discussion in Sec. IV of Tchoufag, Sagaut, and Cambon.²⁸

¹ J. C. Vassilicos, "Dissipation in turbulent flows," *Annu. Rev. Fluid Mech.* **47**, 95–114 (2015).

² N. Mazellier and J. C. Vassilicos, "Turbulence without Richardson-Kolmogorov cascade," *Phys. Fluids* **22**, 075101 (2010).

³ R. Gomes-Fernandes, B. Ganapathisubramani, and J. C. Vassilicos, "Particle image velocimetry study of fractal-generated turbulence," *J. Fluid Mech.* **711**, 306–336 (2012).

⁴ S. Discetti, I. B. Ziskin, T. Astarita, R. J. Adrian, and K. P. Prestidge, "PIV measurements of anisotropy and inhomogeneity in decaying fractal generated turbulence," *Fluid Dyn. Res.* **45**, 061401 (2013).

⁵ K. Nagata, Y. Sakai, T. Inaba, H. Suzuki, O. Terashima, and H. Suzuki, "Turbulence structure and turbulence kinetic energy transport in multiscale/fractal-generated turbulence," *Phys. Fluids* **25**, 065102 (2013).

⁶ R. J. Hearst and P. Lavoie, "Decay of turbulence generated by a square-fractal-element grid," *J. Fluid Mech.* **741**, 567–584 (2014).

⁷ J. C. Isaza, R. Salazar, and Z. Warhaft, "On grid-generated turbulence in the near- and far field regions," *J. Fluid Mech.* **753**, 402–426 (2014).

⁸ P. C. Valente, R. Onishi, and C. da Silva, "The origin of the imbalance between energy cascade and dissipation in turbulence," *Phys. Rev. E* **90**, 023003 (2014).

⁹ S. Goto and J. C. Vassilicos, "Energy dissipation and flux laws for unsteady turbulence," *Phys. Lett. A* **379**(16), 1144–1148 (2015).

- ¹⁰ L. Danaïla, J. F. Krawczynski, F. Thiesset, and B. Renou, “Yaglom-like equation in axisymmetric anisotropic turbulence,” *Physica D* **241**, 216–223 (2012).
- ¹¹ R. J. Hearst and P. Lavoie, “Scale-by-scale energy budget in fractal element grid-generated turbulence,” *J. Turbul.* **15**, 540–554 (2014).
- ¹² P. C. Valente and J. C. Vassilicos, “Universal dissipation scaling for nonequilibrium turbulence,” *Phys. Rev. Lett.* **108**, 214503 (2012).
- ¹³ A. N. Kolmogorov, “Dissipation of energy in the locally isotropic turbulence,” *Dokl. Akad. Nauk. SSSR* **32**, 1 (1941), [*Math. Mech.* **1**, 15–17 (1991)].
- ¹⁴ T. Kármán and L. Howarth, “On the statistical theory of isotropic turbulence,” *Proc. R. Soc. A* **164**, 192–215 (1938).
- ¹⁵ A. N. Kolmogorov, “The local structure of turbulence in incompressible viscous fluid for very large Reynolds numbers,” *Dokl. Akad. Nauk. SSSR* **30**, 9–13 (1941), [*Proc. R. Soc. London* **434**, 9–13 (1991)].
- ¹⁶ Q. Nie and S. Tanveer, “A note on third-order structure functions in turbulence,” *Proc. R. Soc. A* **455**, 1615–1635 (1999).
- ¹⁷ A. Monin and A. Yaglom, *Statistical Fluid Mechanics* (MIT Press, 1975), Vol. 2.
- ¹⁸ P. G. de Gennes, *Introduction to Polymer Dynamics* (Cambridge University Press, 1990).
- ¹⁹ D. Biskamp, *Magnetohydrodynamic Turbulence* (Cambridge University Press, 2003).
- ²⁰ U. Frisch, *Turbulence: The Legacy of AN Kolmogorov* (Cambridge University Press, Cambridge, 1995).
- ²¹ R. A. Antonia and P. Burattini, “Approach to the 4/5 law in homogeneous isotropic turbulence,” *J. Fluid Mech.* **550**, 175–184 (2006).
- ²² W. K. George, “Reconsidering the ‘Local Equilibrium’ hypothesis for small scale turbulence,” in *Turbulence Colloquium Marseille 2011: Fundamental Problems of Turbulence, 50 years after the Marseille 1961 Conference*, edited by H. M. M. Farge and K. Schneider (EDP Sci., Les Ulis, France, 2014).
- ²³ J. Qian, “Slow decay of the finite Reynolds number effect of turbulence,” *Phys. Rev. E* **60**, 3409 (1999).
- ²⁴ F. Moisy, P. Tabeling, and H. Wilaime, “Kolmogorov equation in a fully developed turbulence experiment,” *Phys. Rev. Lett.* **82**, 3994 (1999).
- ²⁵ T. S. Lundgren, “Kolmogorov two-thirds law by matched asymptotic expansion,” *Phys. Fluids* **14**, 638 (2002).
- ²⁶ T. S. Lundgren, “Kolmogorov turbulence by matched asymptotic expansion,” *Phys. Fluids* **15**, 1074 (2003).
- ²⁷ Y. Gagne, B. Castaing, C. Baudet, and Y. Malecot, “Reynolds dependence of third-order structure functions,” *Phys. Fluids* **16**, 482 (2004).
- ²⁸ J. Tchoufag, P. Sagaut, and C. Cambon, “Spectral approach to finite Reynolds number effects on Kolmogorov’s 4/5 law in isotropic turbulence,” *Phys. Fluids* **24**, 015107 (2012).
- ²⁹ R. Schiestel, “Multiple-time-scale modeling of turbulent flows in one point closures,” *Phys. Fluids* **30**, 722 (1987).
- ³⁰ J. L. Lumley, “Some comments on turbulence,” *Phys. Fluids A* **4**, 203–211 (1992).
- ³¹ A. Yoshizawa, “Nonequilibrium effect of the turbulent-energy-production process on the inertial-range spectrum,” *Phys. Rev. E* **49**, 4065 (1994).
- ³² R. Rubinstein and W. J. T. Bos, “On the unsteady behavior of turbulence models,” *Phys. Fluids* **21**, 041701 (2009).
- ³³ R. Kraichnan, “On Kolmogorov’s inertial-range theories,” *J. Fluid Mech.* **62**(2), 305–330 (1974).
- ³⁴ V. Borue and S. A. Orszag, “Local energy flux and subgrid-scale statistics in three-dimensional turbulence,” *J. Fluid Mech.* **366**, 1–31 (1998).
- ³⁵ W. J. T. Bos, L. Shao, and J.-P. Bertoglio, “Spectral imbalance and the normalized dissipation rate of turbulence,” *Phys. Fluids* **19**, 045101 (2007).
- ³⁶ M. Wan, Z. Xiao, C. Meneveau, G. L. Eyink, and S. Chen, “Dissipation-energy flux correlations as evidence for the Lagrangian energy cascade in turbulence,” *Phys. Fluids* **22**, 061702 (2010).
- ³⁷ R. G. Deissler, “Effects of inhomogeneity and of shear flow in weak turbulent fields,” *Phys. Fluids* **4**, 1187 (1961).
- ³⁸ N. Marati, C. M. Casciola, and R. Piva, “Energy cascade and spatial fluxes in wall turbulence,” *J. Fluid Mech.* **521**, 191–215 (2004).
- ³⁹ R. G. Deissler, “Spectral energy transfer for inhomogeneous turbulence,” *Phys. Fluids* **24**, 1911 (1981).
- ⁴⁰ P. C. Valente and J. C. Vassilicos, “The decay of turbulence generated by a class of multi-scale grids,” *J. Fluid Mech.* **687**, 300–340 (2011).
- ⁴¹ P. C. Valente and J. C. Vassilicos, “The nonequilibrium region of grid-generated turbulence,” *J. Fluid Mech.* **744**, 5–37 (2014).
- ⁴² L. H. Benedict and R. D. Gould, “Towards better uncertainty estimates for turbulent statistics,” *Exp. Fluids* **22**, 129–136 (1996).
- ⁴³ M. G. Kendall and A. Stuart, *The Advanced Theory of Statistics* (Charles Griffin & Co. Limited, London, 1958), Vol. 1.
- ⁴⁴ C. Lamriben, P.-P. Cortet, and F. Moisy, “Direct measurements of anisotropic energy transfers in a rotating turbulence experiment,” *Phys. Rev. Lett.* **107**, 024503 (2011).
- ⁴⁵ A. K. Singh and B. S. Bhaduria, “Finite difference formulae for unequal sub-intervals using Lagrange’s interpolation formula,” *Int. J. Math. Anal.* **3**, 17 (2009).
- ⁴⁶ S. Laizet and J. C. Vassilicos, “DNS of fractal-generated turbulence,” *Flow, Turbul. Combust.* **87**, 673–705 (2011).
- ⁴⁷ T. Sjögren, “Development and validation of turbulence models through experiment and computation,” Ph.D. thesis (KTH Royal Institute of Technology, 1997).
- ⁴⁸ T. Sjögren and A. V. Johansson, “Measurement and modelling of homogeneous axisymmetric turbulence,” *J. Fluid Mech.* **374**, 59–90 (1998).
- ⁴⁹ F. Thiesset, R. A. Antonia, and L. Danaïla, “Scale-by-scale turbulent energy budget in the intermediate wake of two-dimensional generators,” *Phys. Fluids* **25**, 115105 (2013).
- ⁵⁰ W. D. McComb, A. Berera, M. Salewski, and S. Yoffe, “Taylor’s (1935) dissipation surrogate reinterpreted,” *Phys. Fluids* **22**, 061704 (2010).
- ⁵¹ S. Laizet, J. C. Vassilicos, and C. Cambon, “Interscale energy transfer in decaying turbulence and vorticity-strain dynamics in grid-generated turbulence,” *Fluid Dyn. Res.* **45**, 061408 (2013).